5-12-2023

# Evaluating the relationship between methane seeps and seafloor geomorphology on the northern US Atlantic margin

Gabriel Hernandez
*Mississippi State University*, gehernandez201@gmail.com

# Evaluating the relationship between methane seeps and seafloor geomorphology on the northern US Atlantic margin

By

Gabriel Hernandez

Approved by:

Adam Skarke (Major Professor)
Padmanava Dash
Qingmin Meng
Andrew E. Mercer (Graduate Coordinator)
Rick Travis (Dean, College of Arts & Sciences)

A Thesis
Submitted to the Faculty of
Mississippi State University
in Partial Fulfillment of the Requirements
for the Degree of Master of Science
in Geosciences
in the Department of Geosciences

Mississippi State, Mississippi

May 2023

Name: Gabriel Hernandez

Date of Degree: May 12, 2023

Institution: Mississippi State University

Major Field: Geosciences

Major Professor: Adam Skarke

Title of Study: Evaluating the relationship between methane seeps and seafloor geomorphology on the northern US Atlantic margin

Pages in Study: 77

Candidate for Degree of Master of Science

Methane seeps are a transport pathway for carbon from seafloor sediments to the marine environment with important implications for global biogeochemical cycling. Accordingly, there is substantial interest in better understanding the processes that control seep location and predicting the distribution of seeps with existing seafloor datasets. Visual evaluation of methane seeps, in multibeam sonar water column data, suggests a spatial relationship between seeps and specific seafloor morphologic features such as ridge crests. In this thesis, seafloor geomorphology at 1996 seep detection sites on the US Atlantic margin was quantitatively characterized by geomorphologic phonotype, bathymetric position index, slope, rugosity, and aspect to evaluate the relationship between seafloor geomorphology and seep location. Results indicate a spatial association between methane seeps and localized bathymetric highs. Additionally, maximum entropy spatial distribution analysis indicates that seafloor geomorphology is partially predictive of seep location and that existing bathymetric datasets may be useful in identifying undiscovered seeps.

ACKNOWLEDGEMENTS

I would like to thank Dr. Adam Skarke, who has been an excellent advisor and an inspiring mentor. I would also like to thank Dr. Padmanava Dash and Dr. Qingmin Meng for serving on my committee as well as being outstanding mentors. All members of my committee have been role models has capable and talented professionals, of which I have benefited from greatly. Finally, I would like to give thanks to my friends and family who have ceaselessly supported me throughout my academic career.

TABLE OF CONTENTS

LIST OF TABLES

LIST OF FIGURES

# CHAPTER I

# INTRODUCTION

## 1.1 Methane Seeps

Methane seeps are locations where methane gas is discharged from seafloor sediments into the ocean. The source of this gas is either biogenic microbial degradation of organic matter in sediments just a few meters (~<10m) below the seafloor or thermogenic generation at deep hydrocarbon deposits thousands of meters below the seafloor (Floodgate & Judd, 1992). As gas migrates from these sources upwards towards the seafloor it is very often, though not always, sequestered for a period in methane hydrate within the seafloor. Methane hydrate is a solid ice-like substance consisting of methane ($CH_4$) gas trapped in a crystal lattice of frozen water (Ruppel, 2011). It is found in the subsurface of the ocean floor within a specific range of depths and temperatures known as the Methane Hydrate Stability Zone (MHSZ), where sufficiently high pressure and sufficiently low temperature enables the hydrate to form in the open pore space between sediment grains (You et al. 2019). Changes in pressure or temperature alter the depth of the MHSZ, affecting the rate of formation and dissociation of methane hydrate, and thus the release of free methane into the ocean. Once methane gas is liberated from hydrate through dissociation, it migrates vertically through the subsurface sediments to the seafloor where is discharged at seeps. The controls on subsurface methane migration are poorly understood but appear to be mediated, in part, by sediment faulting, updip migration through permeable strata,

and intermittent formation and dissociation of hydrate within pore space pathways (Skarke, 2017; Daigle et al., 2020).

Methane seeps are very often hotspots of deep-sea benthic biodiversity with unique microbially generated authigenic carbonate rock outcrops that harbor complex chemosynthetic ecosystems (Figure 1.1) (Levin et al., 2016). Methane emitted at seafloor seeps is used by symbiotic chemosynthetic microbes to fix organic carbon and drive primary production that supports these ecosystems (Turner et al., 2020). These ecosystems often include unique endemic organisms such as chemosynthetic bacteria, mussels belonging to the genus *Bathymodiolus*, and vestimentiferan tubeworms (Levin et al., 2016).

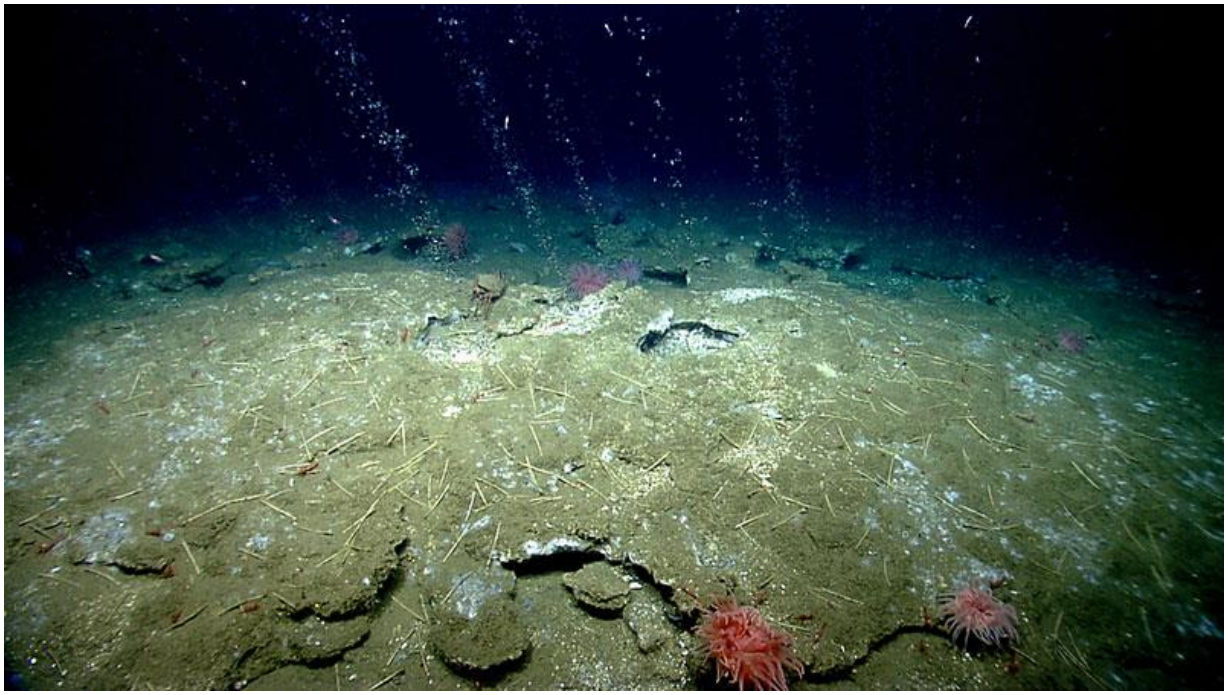

Figure 1.1 Methane bubbles rising out of the seabed at a seep site.

The foreground is largely composed of microbially generated authigenic carbonate rock pavement, which is often observed at methane seep sites. Components of this chemosynthetic ecosystem such as Quill worms, anemones, and patches of microbial mat are visible around the seeps. (NOAA, 2013)

Methane seeps are globally distributed on continental margins (Gardner et al., 2009; Merle et al., 2021; Phrampus et el., 2019; Skarke et al., 2014; Weber et al., 2014); however, their full extent and quantity are not well understood dule to a lack of seafloor mapping data for many parts of the world. On margins where seeps have been detected, they are often found to be concentrated along a depth contour consistent with the very upper limit of the MHSZ zone because hydrate at that depth is especially susceptible to dissolution by minute pressure and temperature changes. (Ruppel, 2011). However, observations indicate that seep locations can vary significantly above and below this depth and the reasons for this are not well understood (Johnson et al., 2015; Skarke et al., 2014).

## 1.2 Importance of Understanding Seeps

The fundamental role of Earth's carbon cycle in global climate variability necessitates a better understanding of the mechanisms that trap and release carbon (Shindell et al., 2009; Dean et al., 2018). Methane seeps are becoming recognized as an important component of the global carbon cycle because they directly link methane hydrate reserves in subseafloor sediments to the marine environment (Davies et al., 2014). Notably, recent estimates indicate that methane hydrate in seafloor sediments is the largest reservoir of free carbon on Earth, sequestering 16-20% of total global carbon (Ruppel & Kessler, 2017). Although methane emitted by modern seeps in water depths greater than ~100 m is not directly emitted to the atmosphere (Ruppel and Kessler, 2017; Joung et al., 2022), the destabilization of the methane hydrate reservoir and the transfer of sedimentary carbon to the active oceanic carbon system has been hypothesized as the cause, and/or a feedback, of rapid global warming episodes in the geological past (e.g. Dickens et al., 1995; Katz et al., 1999; Himmler et al., 2019). Indeed, Quaternary dissociation of methane hydrate is largely due to climate change that has occurred since the last glacial maximum (LGM)

when glacial coverage of the Earth last peaked (Ruppel & Kessler, 2017). Understanding the mechanisms that control the location and variability of hydrate dissociation globally is of great concern to scientists due to the role that methane hydrate dissociation has been suspected to have played in possible exacerbation of past warming events such as the Pleistocene-Eocene Thermal Maximum (PETM) 54.96 Ma ago (Dickens et al., 1995).

Methane released from dissociation of hydrate through seabed seeps drives a wide range of interconnected biogeochemical processes in the shallow subsurface, at the seafloor, and in the overlying water column. These processes contribute to ocean acidification and deoxygenation, resulting in potential hazards for marine organisms and ecosystem health (Biastoch et al., 2011; Kessler et al., 2011). Additionally, methane seeps indicate the potential for significant marine geohazards such as overpressure induced slope failure (Dugan, 2012; Daigle et al., 2020). Finally, they are a demonstrated natural gas energy production resource (Chong et al., 2016; Dugan & Flemmings, 2000) as well as a habitat for commercially viable marine species (Turner et al., 2020).

### 1.3 Knowledge Gap

The location of seeps resulting from hydrate dissociation is theoretically defined by the depth at which the upper limit of the MHSZ intersects the seafloor, and this has been demonstrated in seep detection results at a broadscale (Skarke et al., 2014; Merle et al, 2021). However, at a smaller scale there is notable variability in seep occurrence about this depth, with numerous seeps occurring well above and below the upper limit of the MHSZ (Johnson et al, 2015). This suggests that additional factors, beyond the pressure/temperature stability of hydrate, may exert control on the localized seafloor discharge location of dissociated methane. As noted, the transport pathway that dissociated methane take to the seafloor may be influenced by

sediment faulting, updip migration through permeable strata, and intermittent formation and dissociation of hydrate within pore space pathways, which may in turn be related to seafloor morphological expression; however, these processes and their implication for gas migration are not well understood (Skarke, 2017; Daigle et al., 2020).

Analysis of multibeam sonar water column backscatter data from hundreds methane seeps along the United States Atlantic margin indicates that seeps may be spatially associated with specific seafloor morphologic features such as ridge crests and other localized bathymetric highs. If an association between seafloor geomorphology and seep location exists, it may yield greater insight into the geologic processes that control the subsurface vertical migration pathways of gas between its source or points of hydrate dissociation, and locations of seafloor discharge. Additionally, if an association is established between the presence of seeps and seafloor geomorphology, it could be integrated with an improved understanding of the geologic controls on shallow methane migration to predict the most likely location of seeps on unexplored margins and those that have been bathymetrically mapped but lack water column observations, thus improving the efficiency of future seep detection and mapping efforts.

### 1.4 Research Objective and Hypothesis

Based upon the stated knowledge gap, the goal of this thesis is to evaluate the degree of spatial association between seep locations and quantitative measures of seafloor geomorphology using seafloor properties derived from bathymetric data recorded on the United States Atlantic Margin (USAM). Specifically, I will evaluate the statistical association of seep presence with geomorphological form as classified by geomorphologic phonotypes, bathymetric position index, rugosity, slope, and aspect. Additionally, I will evaluate the degree to which geomorphological form is predictive of the presence of seeps using maximum entropy spatial distribution analysis.

Based upon preliminary results and visual analysis of multibeam sonar data with detected seeps, I hypothesize that methane seeps on the USAM have the greatest spatial correlation with bathymetric high points.

# CHAPTER II

# BACKGROUND

## 2.1 Seep Processes

Methane hydrate is an ice-like solid substance that consists of gaseous methane molecules trapped in a crystal lattice of frozen water. It is found in much of the world's sedimentary seafloor subsurface at ocean depths greater than 300 to 500 meters (Dillon et al. 1993). This hydrate serves as a large reservoir for seafloor methane, which originates from either thermogenic processes, vertically migrating thousands of meters from deep hydrocarbon deposits, or biogenic processes, resulting from microbial biodegradation of organic matter within tens of meters of the seabed (Floodgate & Judd, 1992). When methane is generated within, or migrates to, an area of the subsurface with sufficiently high pressure (3-5 MPa) and sufficiently low temperatures (< 25˚ C), ice-like crystals will grow and trap methane molecules in a crystal lattice, forming methane hydrate (Ruppel, 2011; Judd, 2003). In addition to necessary pressure and temperature conditions, hydrate also requires sufficient pore water to form ice and sufficient methane concentrations above solubility within that pore water (Ruppel and Kessler, 2017).

Methane hydrate is formed and persists within seafloor sediment pore space, until pressure and/or temperature conditions move outside threshold values necessary for hydrate stability, and dissociation (i.e. melting of ice lattice) occurs, resulting in the release of free methane gas. This methane gas can then escape the seabed at a seep site and form gas plumes in the water column above. Although methane seeps are commonly a result of dissociation of

methane hydrate, it should be clarified that not all methane seeps are, as some seep sites are found in locations where temperature and pressure conditions as well as water availability are not sufficient for hydrate to form. In these cases, thermogenic and biogenic methane migrate from their source to seafloor seeps as free gas.

A variety of factors that control ocean pressure, temperature, and methane solubility influence the stability of methane hydrate including tidal and eustatic sea level variations, as well as changes in deep ocean temperature and salinity (Klauda & Sandler, 2005; Romer et al., 2016). A specified vertical range of temperature and pressure constitutes the methane hydrate stability zone (MHSZ) with the upper limit typically residing between 300 and 500 meters below sea level (mbsl) (Ruppel, 2011; Römer et al., 2016) and the lower limit being highly dependent on geothermal gradient beneath the seafloor and available methane in the region, but typically residing around 3000 mbsl (Klauda & Sandler, 2005; Dickens et al., 1995). Once dissociation liberates free methane into the pore space of seafloor sediments, its migration pathway to the seafloor may be impacted by variability in sediment permeability, sediment faulting, and sediment bedding orientation. Updip migration of free gas along the bedding planes of sedimentary layers has been hypothesized as a subsurface migration mechanism that could influence the seafloor position of gas discharge (Ruppel, 2011) and may have a relationship with seafloor geomorphology.

## 2.2 Seep Distribution

Methane seeps have been found in a wide range of marine environments around the world (Phrampus et al, 2019), having been observed on active margins such as the U.S. Cascadia Margin (Merle et al., 2021), as well as passive margins like the Mid-Norwegian Continental Margin (Naehr et al., 2007) and USAM (Skarke et al, 2014). They have also been observed in

isolated basins such as the Black Sea, where changes in salinity have caused destabilization of hydrate bearing sediments (Riboulot et al., 2018). Since methane seep distribution is confined by available methane, which itself is confined by available organic carbon, the possible range of seep presence is somewhat narrowed to regions with sediment that is sufficiently supplied with such carbon. Besides the availability of carbon, factors such as depth (bathymetry) play a primary role in the constraints on global methane seep distribution (Phrampus et al., 2020), which is a reason why a majority of seeps are found on or around continental margins. Notably, most recordings of seep presence have not been in polar latitudes, but this may be a bias that is due to a lack of surveying in more remote regions. Furthermore, we can expect that much of what we know about seep distribution at the present could be biased by limited survey locations.

### 2.3 Biogeochemical Pathways

As mentioned previously, seeps are only present in regions with sufficient available carbon. The methane that seeps consist of is produced in the subsurface either biogenically through microbial methanogenesis and alkanogenesis (Hinrichs et al., 2006) or thermogenically through catagenesis and metagenesis as a result of heat from the geothermal gradient and pressure from the sediment and water overhead (Abrams, 2005). The methane produced by these processes is able to travel through faults which connect hydrocarbon reservoirs deep in the sediment with the water column above. Isotopic analysis of samples collected at seeps on the US Atlantic margin indicate that the methane emitted from hydrate on this margin has a microbial origin (Prouty et al. 2016). Much of the methane produced by this process will be either trapped within the porous sediment or will rise to the seabed, with a substantial portion of it being anaerobically oxidized during migration (Judd, 2003). In addition to oxidation, this methane is undergoing authigenic carbonate mineralization during its upward migration (Joye, 2020). The

methane that reaches the seabed, is ejected into the water column, where the plume can rise hundreds of meters before being dissolved into the water, at the depth of the upper limit of that MHSZ, preventing it from reaching the ocean surface. The persistence of the bubbles in the ocean water column is a result of a thin methane hydrate shell on the outside of each bubble, which greatly slows methane gas dissolution into the ocean between the seafloor and the depth of the upper limit of the MHSZ, at which point the hydrate shell dissociates and the gas bubble dissolves in to the seawater (Fu et al., 2021). After this dissolution, the methane present in the bubbles ends its journey and undergoes aerobic microbial oxidation, where methanotrophic bacteria consume and oxidize the available methane, consuming dissolve oxygen and producing carbon dioxide (Ruppel & Kessler, 2017; Valentine et al, 2001).

### 2.4 Seafloor Data and Seep Detection

This analysis relies on bathymetric data covering a large portion of the United States Atlantic Margin between Cape Hatteras and George's Bank. These data were recorded using multibeam echosounder sonar. This instrument emits seismic pressure waves (i.e. sound waves) from a transducer array on the bottom of a ship, ensonifying a volume of the ocean beneath the ship, which can be resolved to a fan shaped profile through beam forming (Lurton, 2010) (Figure 2.1). These sound waves travel from the vessel to the seafloor where they are reflected back to the ship. The return from these sound waves provides two main types of information: The amount of time it takes for the seismic pulse to return to the transducer, and the intensity of that return. The amount of time it takes for the pulse to return will provide a precise estimation of depth along each beam, assuming the sonar is provided with the correct speed of sound in the water that is being surveyed. The intensity of the return (backscatter) provides information regarding the acoustic impedance of the interface that pulse is reflecting off of. In the case of the

seafloor, the acoustic impedance of the seafloor is significantly greater than that of the overlying water creating a strong reflection that indicates the depth of the ocean along a profile beneath the ship. In the case of gas bubbles in the water column above the seafloor, the acoustic impedance of the gas is significantly greater than that of the surrounding water creating a strong reelection that indicates the presence of bubbles and can be used to identify the location of gas bubble plumes which can be used to identify the location of their seafloor gas seep source (Figure 2.1). Taken in succession, these sonic pulses produce data that can be represented as a bathymetric surface as well as a fan view of the water column. When these data are combined and processed, they provide a complete bathymetric map of the surveyed area, such as the map being used in this thesis to evaluate seafloor bathymetry (Figure 2.2) (USGS, 2016).

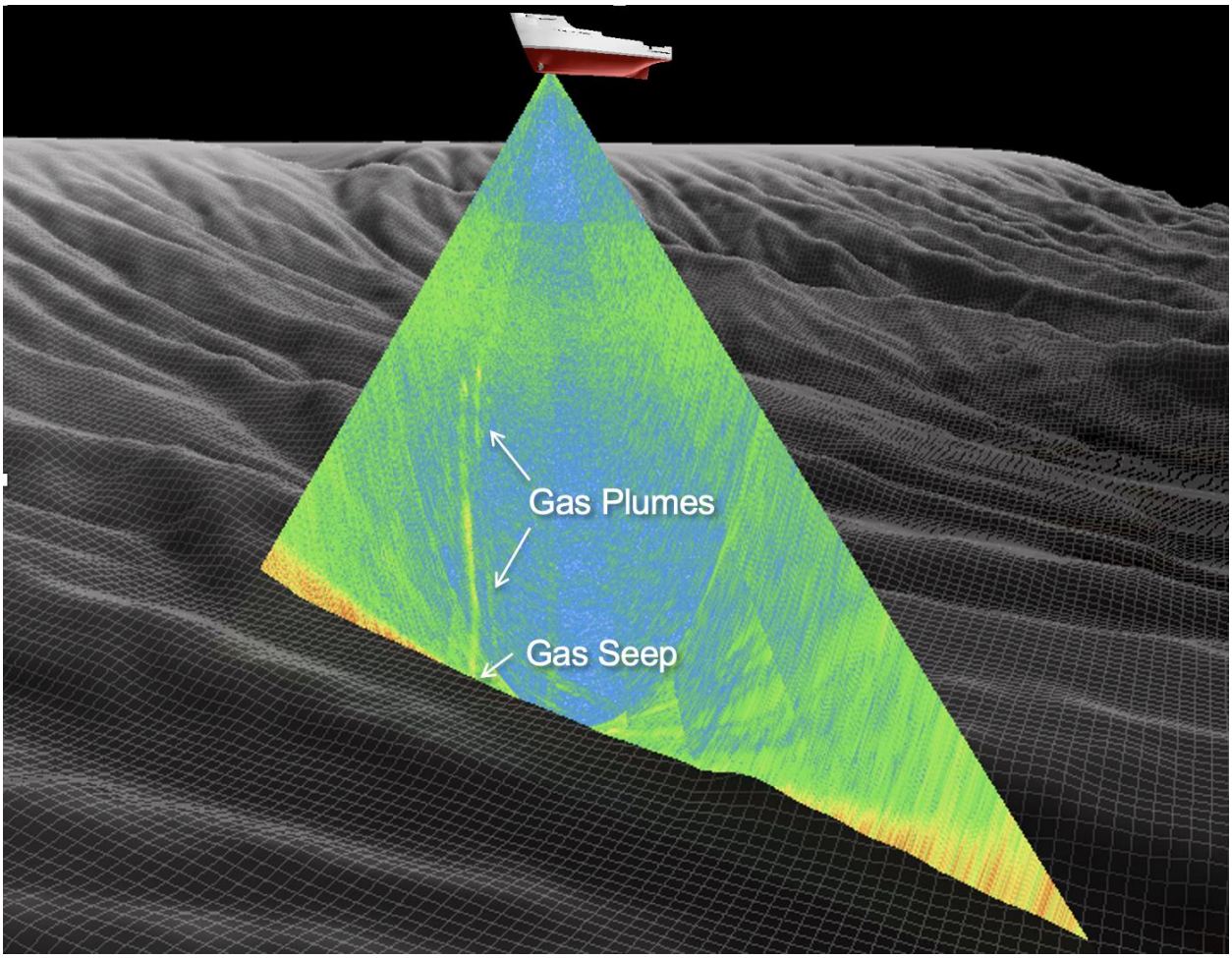


Figure 2.1 Diagram of multibeam sonar fan beam beneath ship.

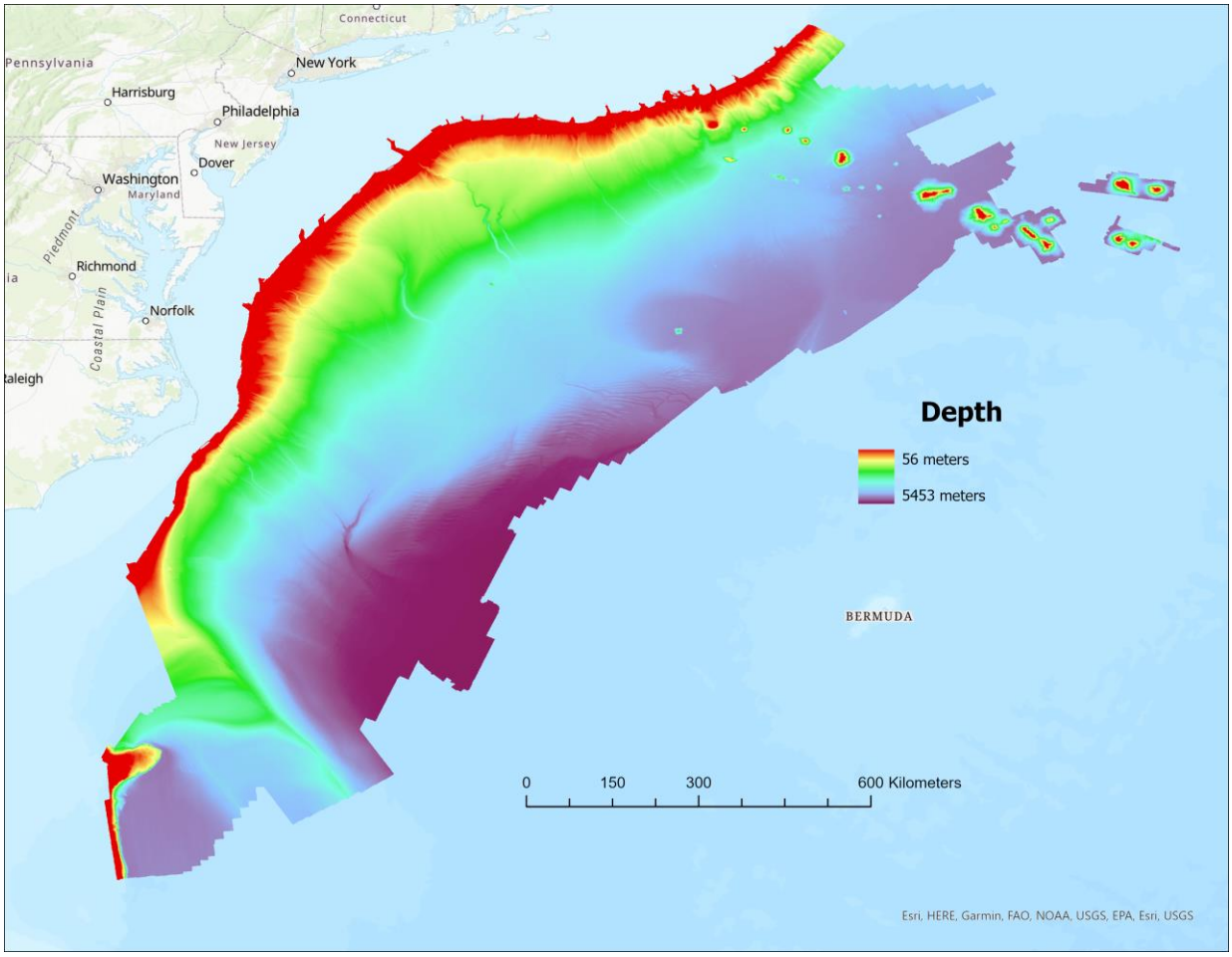


Figure 2.2 Bathymetric map of the survey area on the United States Atlantic Continental Margin between Cape Hatteras and Georges Bank. (Andrews et al., 2016)

A series of multibeam sonar survey cruises, conducted between 2011 and 2019 on the NOAA ship *Okeanos Explorer*, have produced a water-column acoustic backscatter dataset for the northern US Atlantic Margin. Utilization of water column sonar data not only allows for precise detection of seafloor seep sites, but also the analysis of the vertical structure of the gas plumes that the seeps produce and the effect they have on ocean stratification as these plumes can rise to depths on the order of hundreds of meters (Skarke et al., 2014). The acquisition of this water column dataset allowed for manual visual interpretation of seep presence using software

included in the QPS suite such as Fledermaus and FMMidwater, which produced precise seafloor coordinates for each seep site. These coordinates were imported as a point layer in QGIS and ArcGIS, allowing for their use in analysis (Figure 2.3).

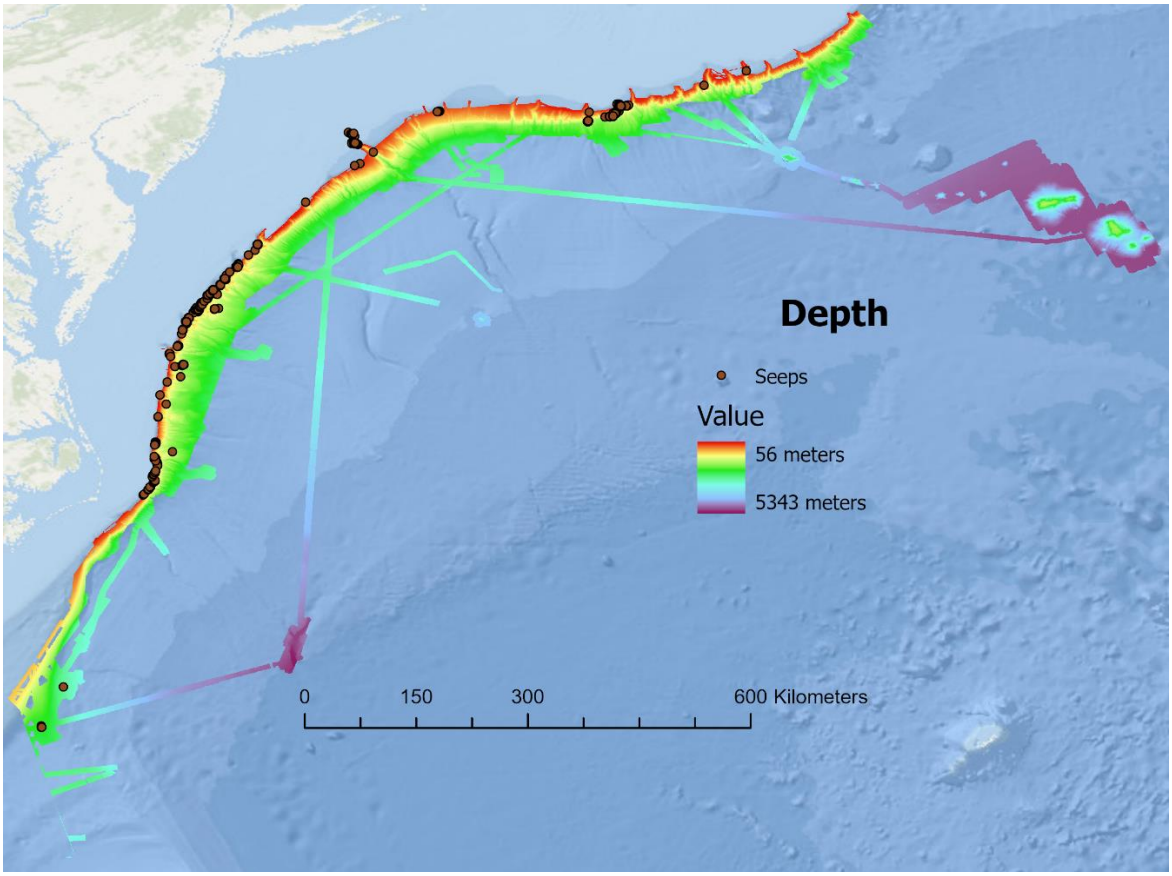


Figure 2.3 The study area trimmed by available survey coverage with orange points marking seep locations.

## 2.5 Geomorphology

The geomorphologic controls on, or results of, seep presence aren't well understood, so it is important to consider a variety of methods to quantitatively classify seafloor geomorphology in order to evaluate it relationship with seeps. The first approach was to use geomorphologic

phonotypes (geomorphons) following the approach of (Jasiewicz & Stepinski, 2013). Conceptually, geomorphons are units of terrain that are classified by their general shape. A function that utilizes this classification scheme was integrated as a tool into QGIS geospatial software (Stepinski & Jasiewicz, 2011). The classification method utilizes the recorded elevations of 8 equidistant points surrounding a center point. These 8 points are determined to be higher, lower, or equal in elevation to the center point (Figure 2.4). The orientation of the combined 8 points is then designated as matching with one of the already specified geomorphons. A broader classification scheme includes 498 geomorphologic phonotypes, but the *r.geomorphon* function used in QGIS reduces the classification into 10 more generalized geomorphologic phonotypes (Flat, Peak, Ridge, Shoulder, Spur, Slope, Pit, Valley, Footslope, and Hollow) (Figure 2.6). The function is designed to attribute a specific geomorphologic phonotype to individual raster cells, allowing for a visualization of their distribution in a map (Jasiewicz & Stepinski, 2013) (Figure 2.5). Using this tool, general trends in landform types across a dataset data set can be identified and interpreted to inform analysis.

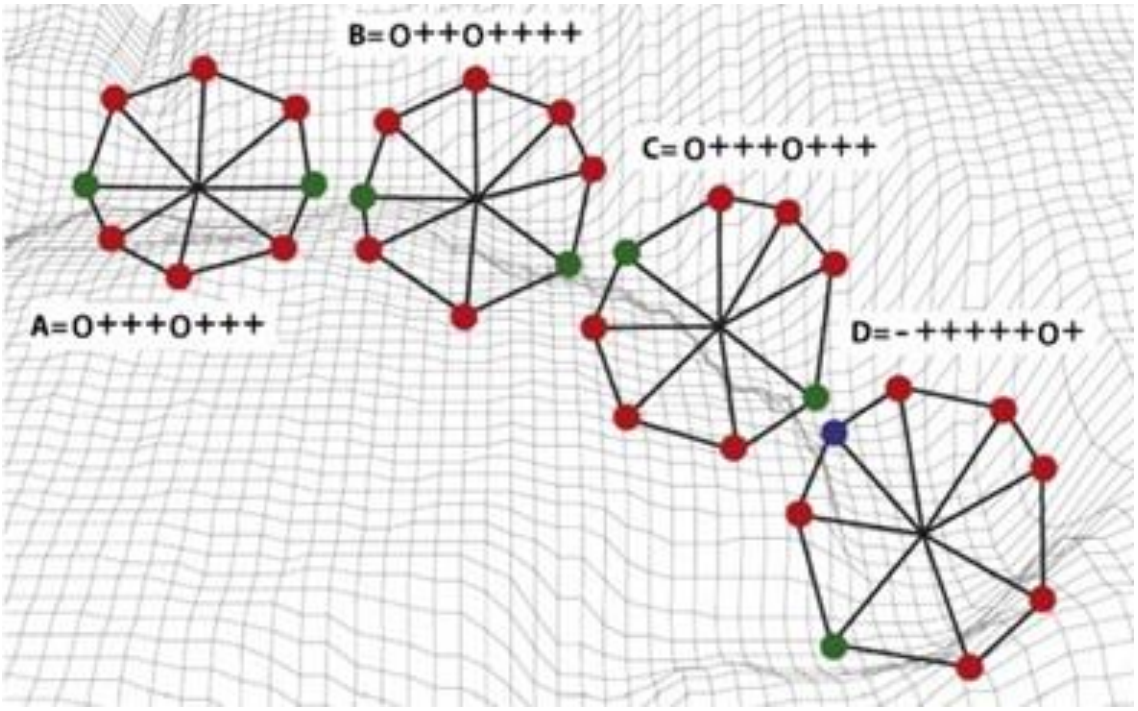


Figure 2.4 Example of the function behind geomorphon classification, designating 8 surrounding points as higher (red, +), lower (blue, -), or equal (green, 0) in elevation to the central point. (Jasiewicz & Stepinski, 2013)

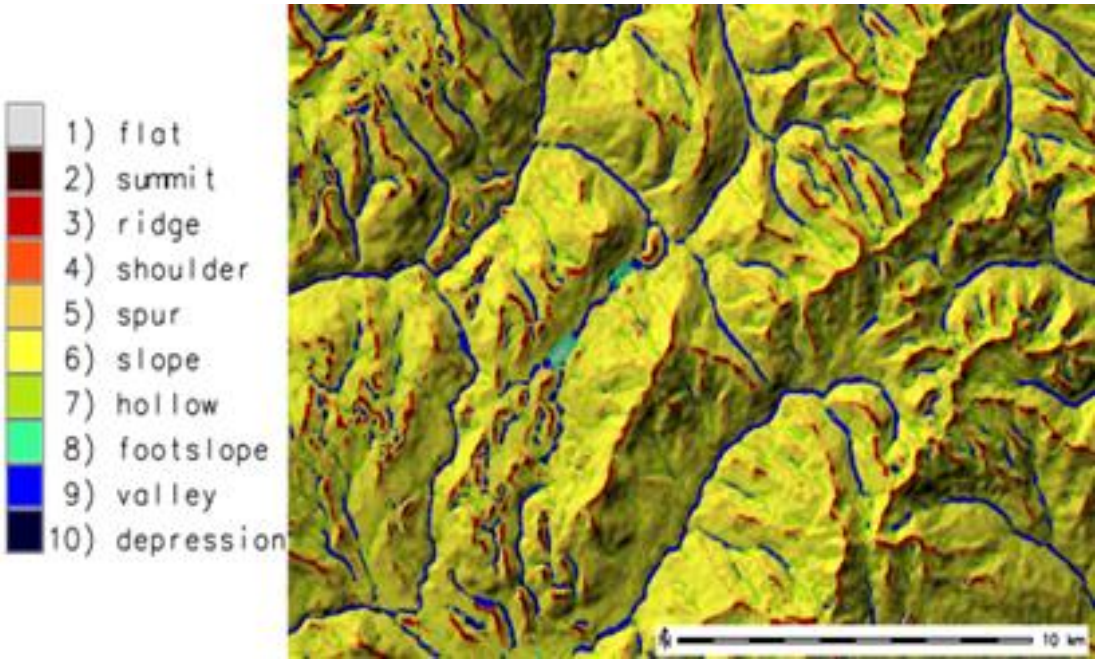


Figure 2.5 Geomorphons listed and layered over a digital elevation model. (osgeo, 2021)

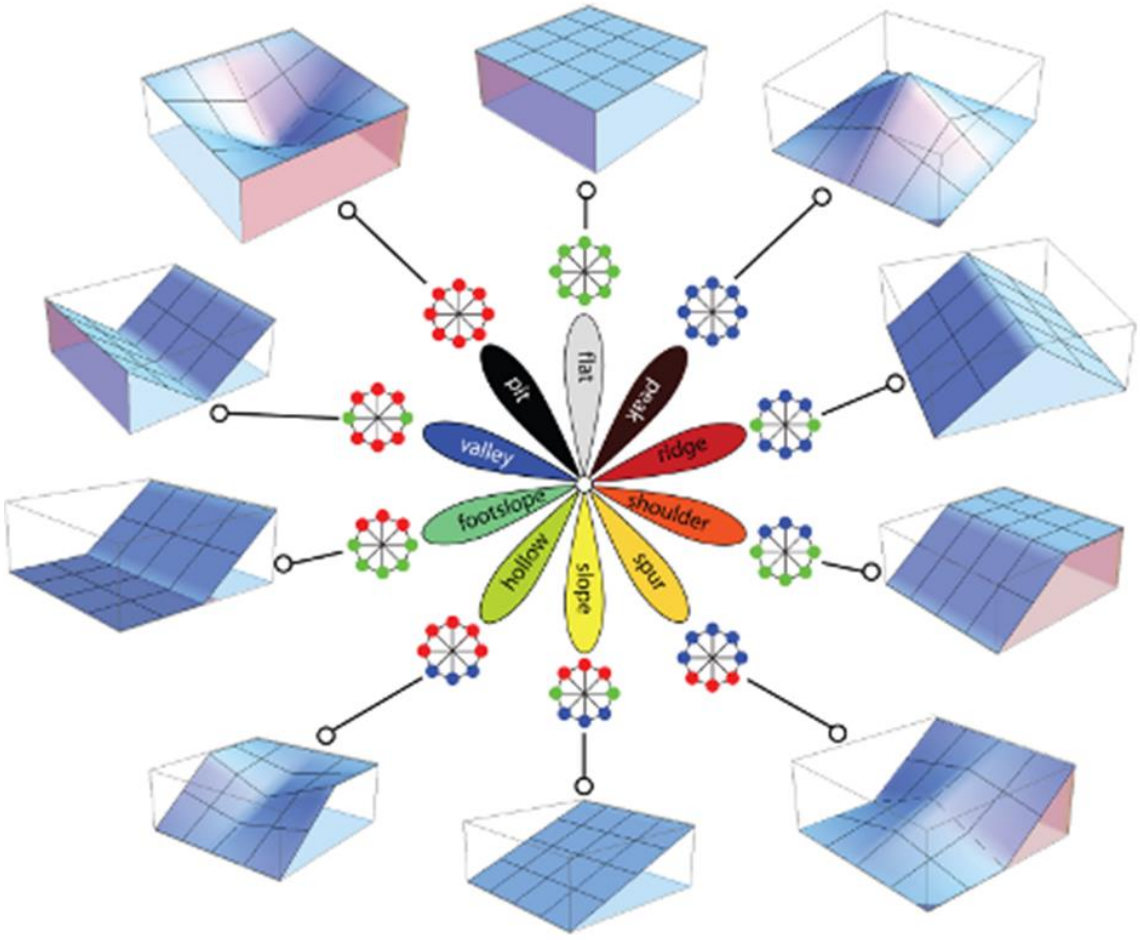


Figure 2.6 The classification scheme applied to sites based on positioning of surrounding points following the same legend as in Figure 4.2. The words “summit” and “depression” are used in Figure 4.2 and the words “peak” and “pit” (respectively) are used here, but in this case these terms are synonymous. (osgeo, 2021)

Another approach to classifying seafloor features is the Bathymetric Position Index (BPI). BPI was derived from the Topographic Position Index (TPI) which classifies topography according to slope position and landform type (Walbridge et al., 2018; Weiss, 2001). This process is done by comparing the elevation of individual cells in a digital elevation model with the mean elevation of a specified radius of surrounding cells (Figure 2.7). Positive values indicate positions that are higher in elevation than surrounding positions, negative values

indicate positions that sit lower than surrounding positions, and values near zero indicate flat surfaces or constant slopes. This method of classification is utilized in the Benthic Terrain Modeler (BTM) which is available as a set of tools in ESRI ArcGIS. The BTM allows for a wide variety of classification as the results produced by the toolset are highly dependent on scale. When compared with the geomorphon classification system, the BPI allows for a higher specification of classification depending on the scale of the seafloor features being observed. Additionally, the BPI can derive rugosity in a grid from an input bathymetric dataset, relying on a neighborhood analysis using a 3x3 grid cell neighborhood. Utilizing an ordinal scale instead of a nominal scale will allow for a more detailed classification that won't be restricted to 10 classes (Figure 2.8).

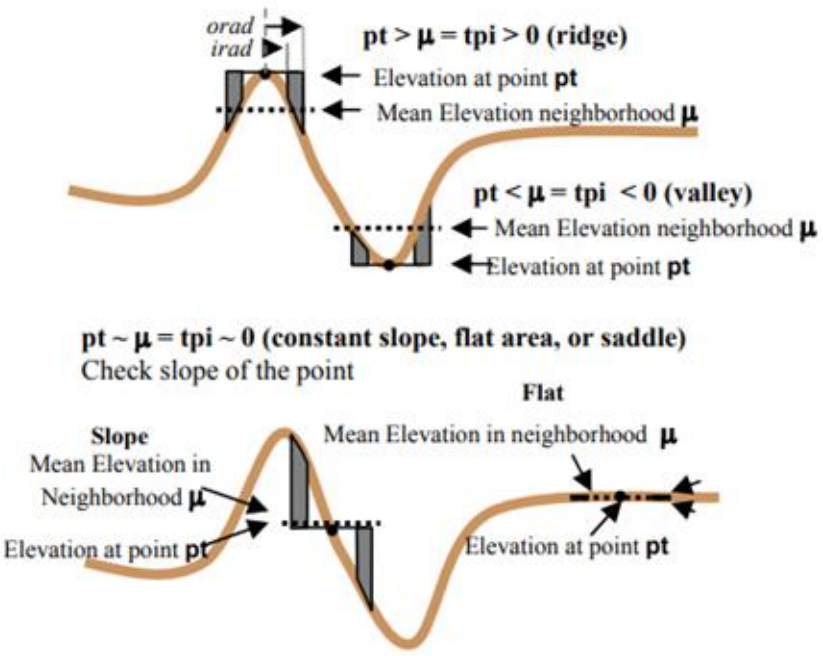


Figure 2.7 Mean elevation of an annulus neighborhood surrounding specified points provide a classification of slope position and landform type. (Weiss, 2001)

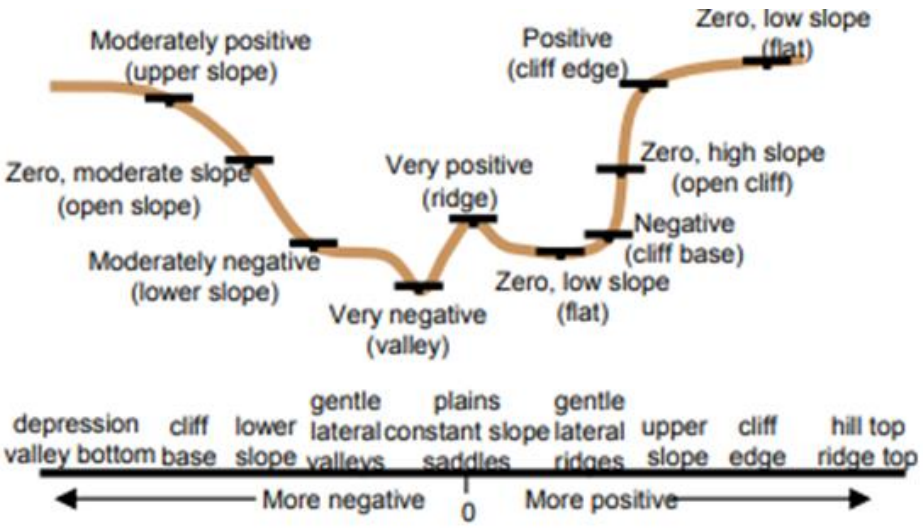


Figure 2.8 Landforms are classified into slope position classes using TPI values on a continuous scale. (Weiss, 2001)

In addition to geomorphons and BPI, variables such as slope, rugosity, and aspect were included in the analysis to investigate if any relationship exists between seep position and these parameters that quantitatively describe characteristics of seafloor geomorphology. Slope is the measure of the degree of steepness of a surface relative to a horizontal plane. The measure of slope in a given area can provide insight into the geological processes present, as erosional and depositional forces will play out differently on steeper or flatter surfaces. This is especially relevant to seep processes as the upward movement of gas through sediment can differ based on variations of slope.

Rugosity is the measure of how morphologically dynamic a surface is (i.e. how rough or smooth). The greater the variability in amplitude of elevation within a surface, the higher rugosity it has. The degree of seafloor rugosity surrounding seeps can, like slope, reveal relationships present between seep emergence and the geomorphology of the seafloor. A higher

rugosity around seep sites could imply that seeps are more likely to emerge in specific environments that are more dynamic in their fine scale variations in elevation, or that seep processes increase the variability of seafloor elevation through the generation of features like authigenic carbonate rock outcrop.

Finally, aspect is the measure of directionality of a surface relative to cardinal and intercardinal directions. When examining the face of a surface, the aspect can be determined by comparing it to the geodesic azimuth (directional angle in a spherical system). This provides a measurement of the angle between the direction the surface is facing and geographic north. The relationship between prevailing ocean currents and bathymetry could result in consistent azimuthal) orientation of seafloor location s with seeps (e.g. consistent seepage on up current side of continental slope ridges relative to the down current side due to differential sediment erosion and deposition rates).

## 2.6 Maximum Entropy Distribution Modeling

Maximum Entropy (Maxent) is a statistical method of predictive modeling of the distribution of a subject (feature or species) in a given area. Maxent modeling makes use of the Maximum Entropy Principle, which states that the most representative probability distribution of samples in a system is the one with the largest entropy (Jaynes, 1957). This method of distribution modeling examines the known distribution of a subject in an area and compares it with a set of identifiable environmental constraints (explanatory parameters) on said distribution, specifying what regions of that area are likely to contain the appropriate combination of constraints to allow for possible presence. Since this method of modelling is susceptible to overfitting of training data, regularization is applied to reduce explanatory variable coefficients. This process can remove the influence of less relevant variables and allow the model to be more

applicable to differing datasets. Additionally, cross-validation is applied to the model to evaluate its performance on differing datasets.

The approach has several advantages that prove beneficial to the requirements of this research. It only requires presence data for whatever feature or species is being modeled, which is important because absence data can be difficult to obtain in certain contexts, especially within regions that cover a large geographic area. This is generally true for the seep data used herein since seeps exhibit temporal variability making it impossible to confirm seep absence based on a single observation in time. Additionally, the maxent approach can use both continuous and categorical data to train a model (Phillips et al., 2006), so geomorphons (categorical) can be incorporated into the training of the model along with BPI, slope, rugosity, and aspect (continuous). This approach is most commonly used in the modeling of the distribution of a biological species, but seep presence on a continental margin serves as an analogous situation in which Maxent has substantial utility.

# CHAPTER III

# METHODS

## 3.1 Seep Database and Seafloor Bathymetry

The focus of the first stage of this research was to ensure that all data would be appropriately displayed and prepared for analysis. First, both the bathymetric data (Andrews et al., 2016) for the survey area (Figure 2.2) and the coordinates for 1,996 detected seep sites (Skarke et al, 2014; Skarke et al., 2018) within that area were imported as a raster layer and a point layer respectively in both ArcGIS and QGIS. This bathymetry was specifically chosen due to its wide coverage of the continental margin (89,368.32 $km^2$) that overlaps with a substantial dataset of identified seep locations (Figure 2.3). The seep detections were made by identifying gas bubble plumes in the water column imaged with a multibeam echosounder as described in the background section and following the approach of Skarke et al. (2014, 2018). There were some regions of the original bathymetry that were not covered in any of the survey cruises that recorded the water column data which the seeps were found in, so any bathymetry that fell outside of the covered area was cut.

## 3.2 Geomorphologic Phonotypes

The first phase of the classification process was completed using the *r.geomorphon* function applied in QGIS. The function requires a defined outer search radius (OSR) which defines the seafloor surface area around a DEM cell, from which bathymetry data is analyzed to yield a geomorphon class that is assigned to that central DEM cell. Because the geometric

analysis used to classify geomorphology with *r.geomorphon* is scale dependent, the data were initially processed with a series of OSR to investigate the sensitively of the geomorphic classification for the full survey area to variation in OSR . To do this, the study area DEM (Andrews et al., 2016) was analyzed with *r.geomorphon* using a range of search radii from 1-50 cells (0.1-5 km) which resulted in each cell being assigned a geomorphon class based on analysis of 0.03 – 78.54 $km^2$ of surrounding seafloor. This analysis produced different geomorphon class distributions for the full survey area for every search radius (Figure 3.1)**.** Each plot exbibits substantial variability at low search radius values, which generally becomes more stable as the radius values increase. However, there is not a singular search radius where all plots demonstrate stability. Accordingly, three separate OSR values (5 cells, 15 cells, and 25 cells) were selected for use in analyzing the association of geomorphons and seeps in order to evaluate the sensitivity of the resultant associations to the selected *r.geomorphon* search radius. A search radius of 5 cells (0.5 km), yielding an analyzed seafloor area of 0.8 $km^2$, was selected for use in analysis because the OSR analysis (Figure 3.1) suggests that an OSR above 5 cells reduces resolution but does not significantly change geomorphon values while an OSR below 5 cells produces values that vary too widely. The product was a raster layer classifying the margin by geomorphon (Figures 3.2 and 3.3). The geomorphon values of cells containing points representing seep sites were then sampled to compare the frequency of geomorphon class occurrence at seep sites relative to the whole survey area.

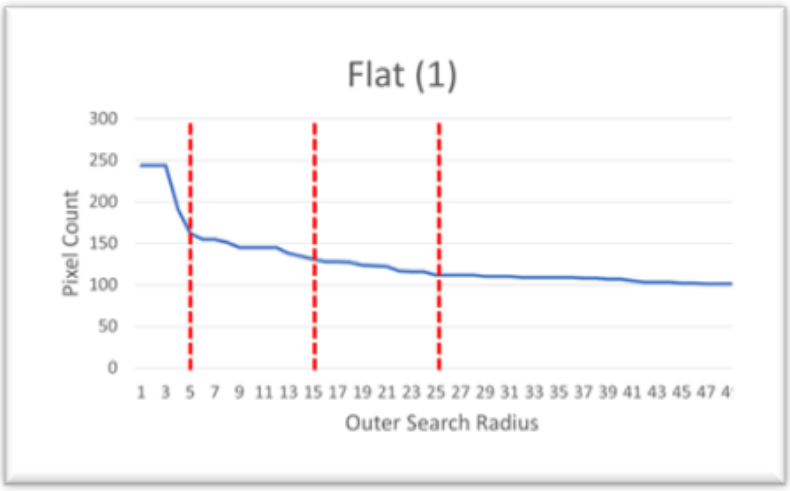


Figure 3.1 Ten plots showing the difference in pixel counts for each geomorphic class in the DEM for the USAM (Andrews et al., 2016) as a function of outer search radius value (1-50)


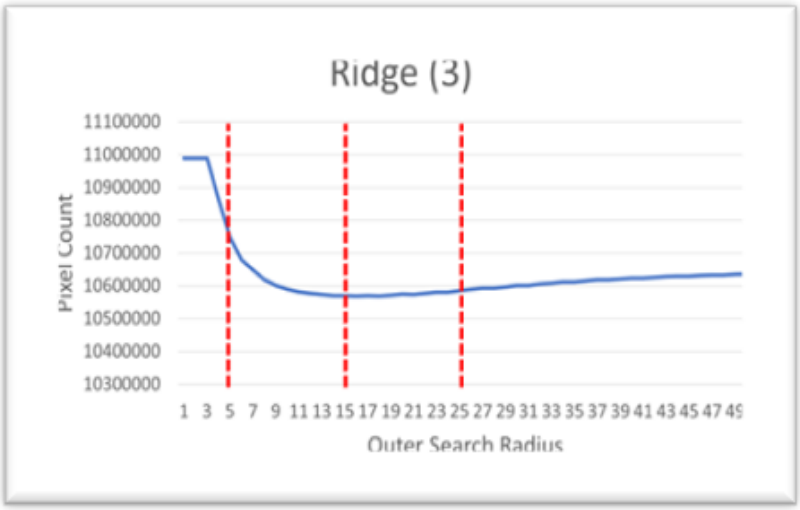


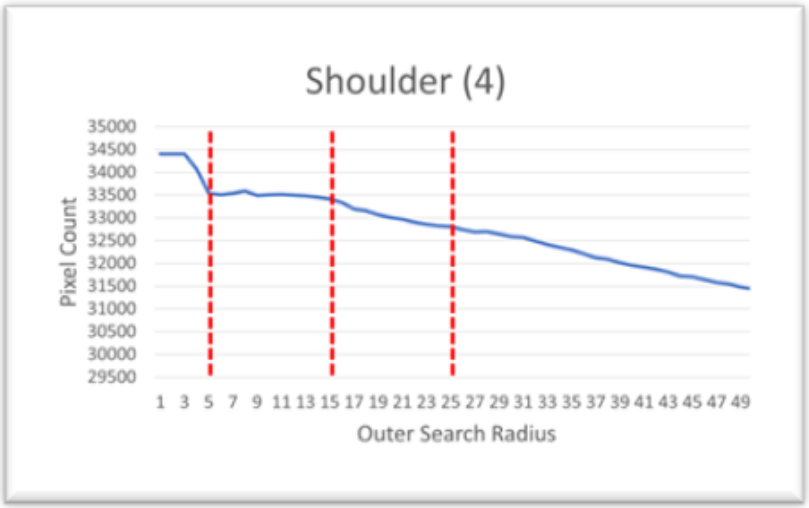


Figure 3.1 (continued)

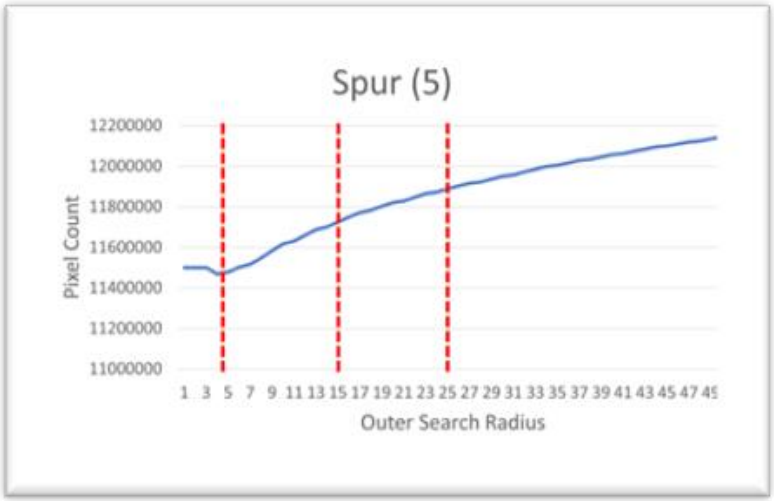


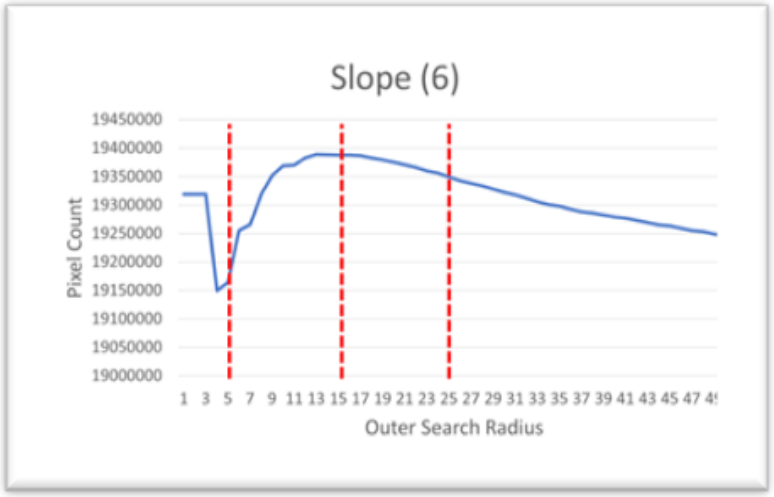


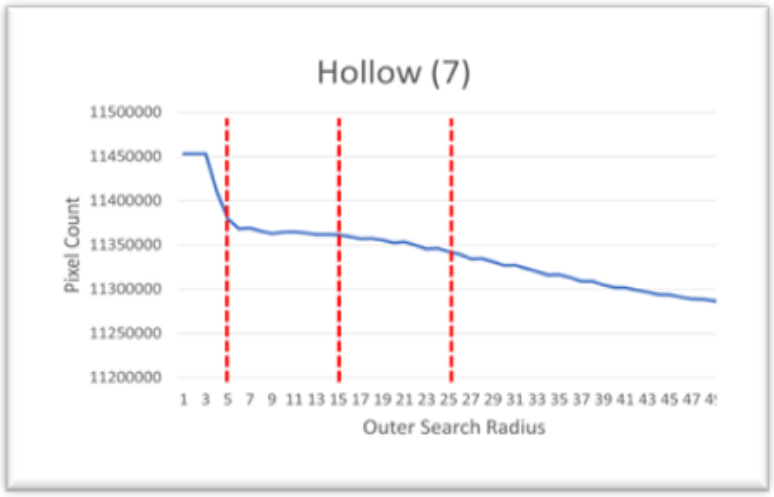


Figure 3.1 (continued)

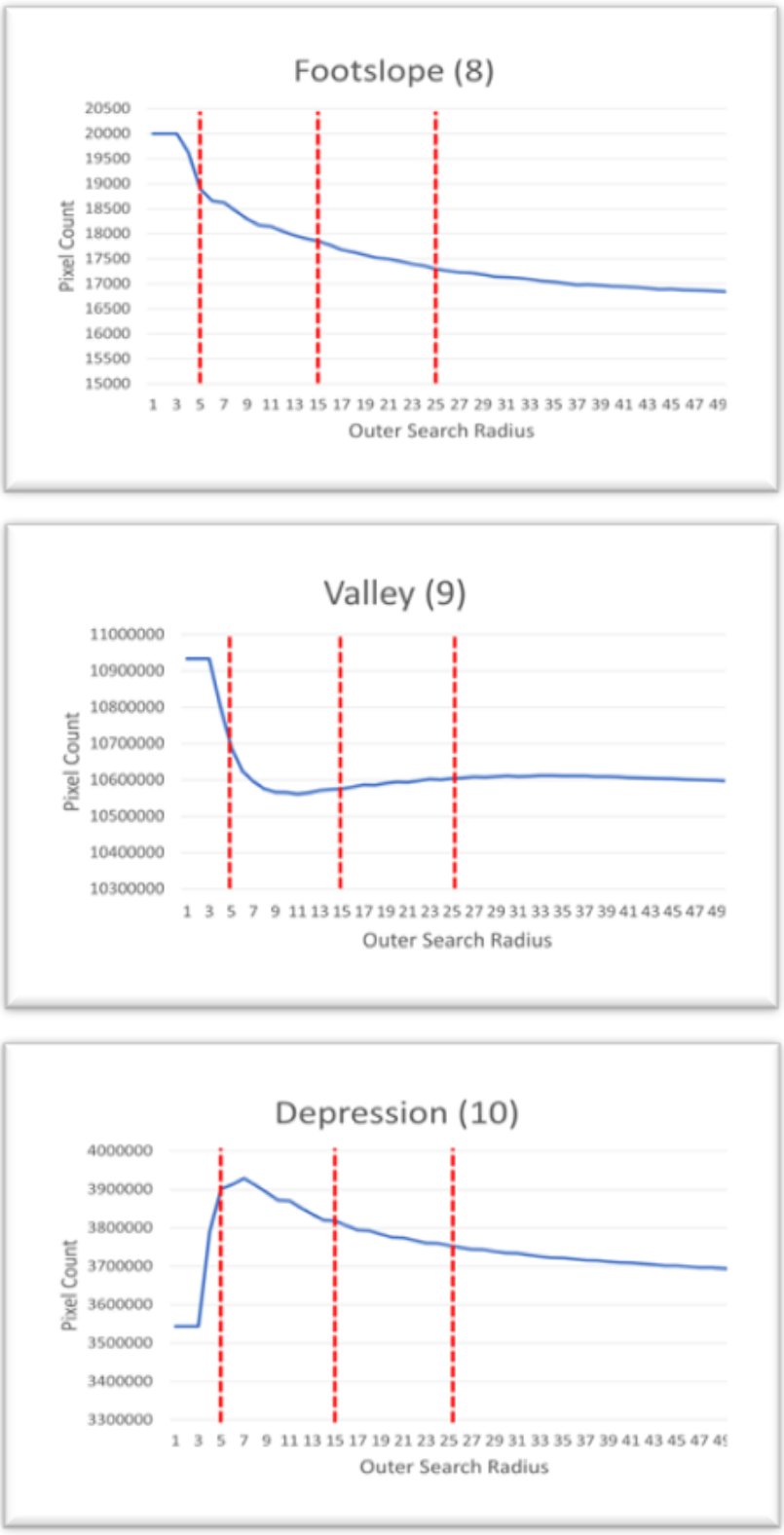


Figure 3.1 (continued)

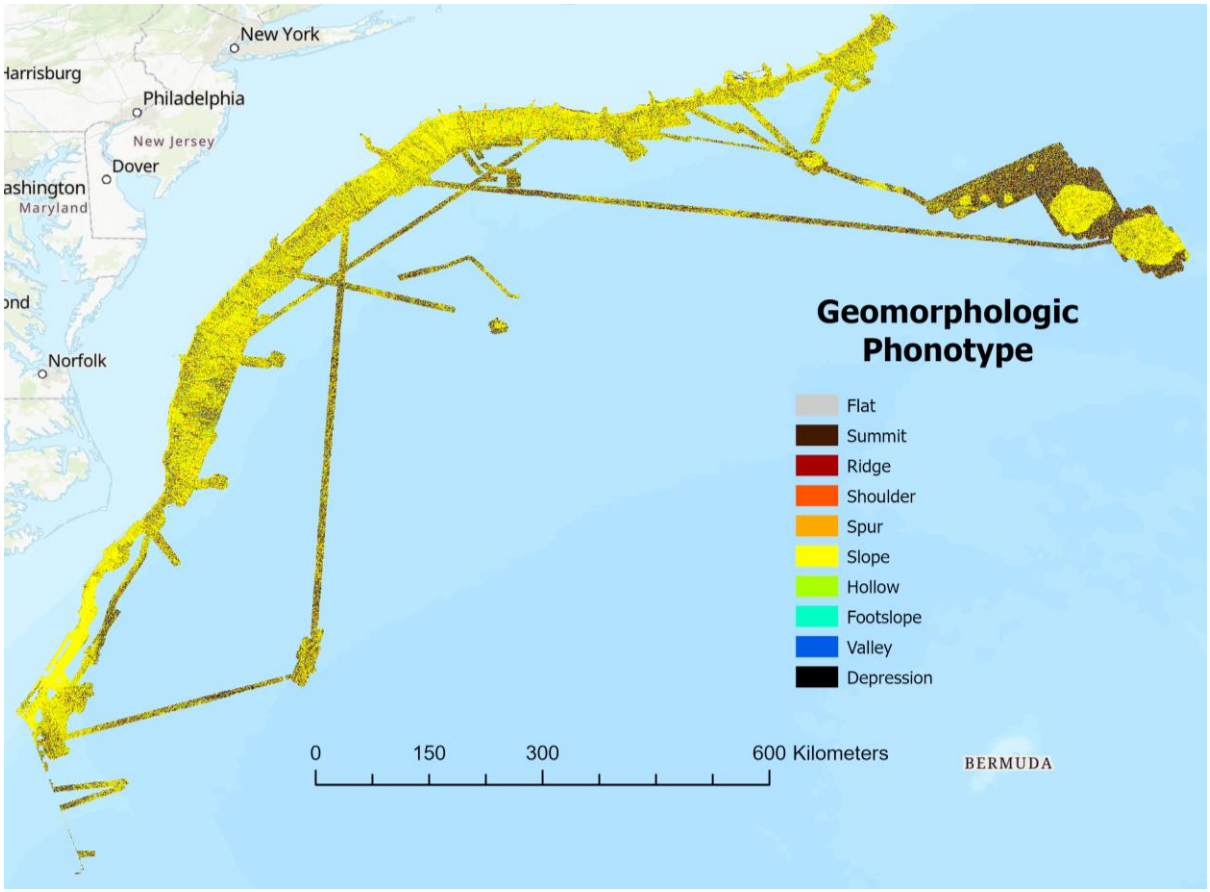


Figure 3.2 Survey area on the United States Atlantic Margin classified by geomorphologic phonotype.

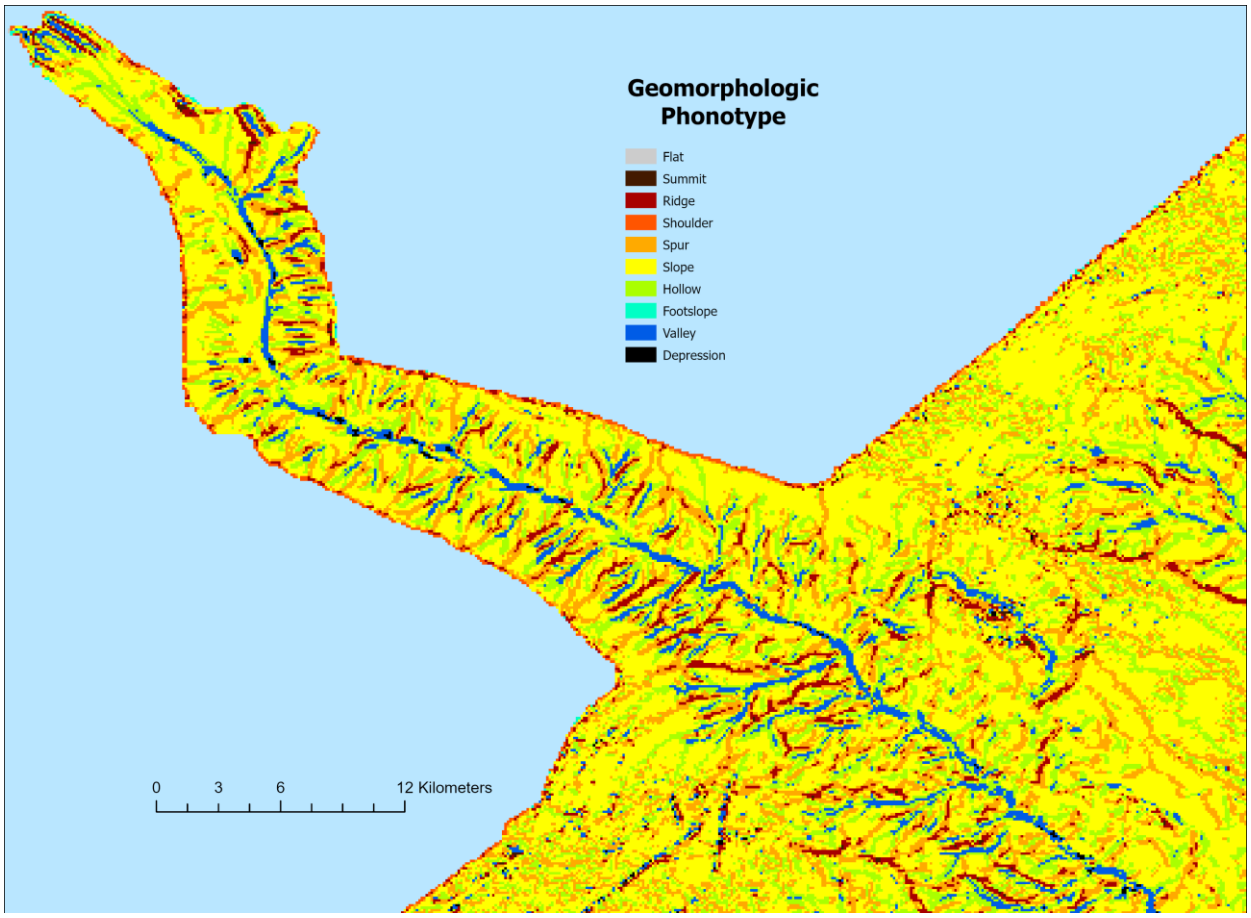


Figure 3.3 Hudson canyon region of the survey area classified by geomorphologic phonotype.

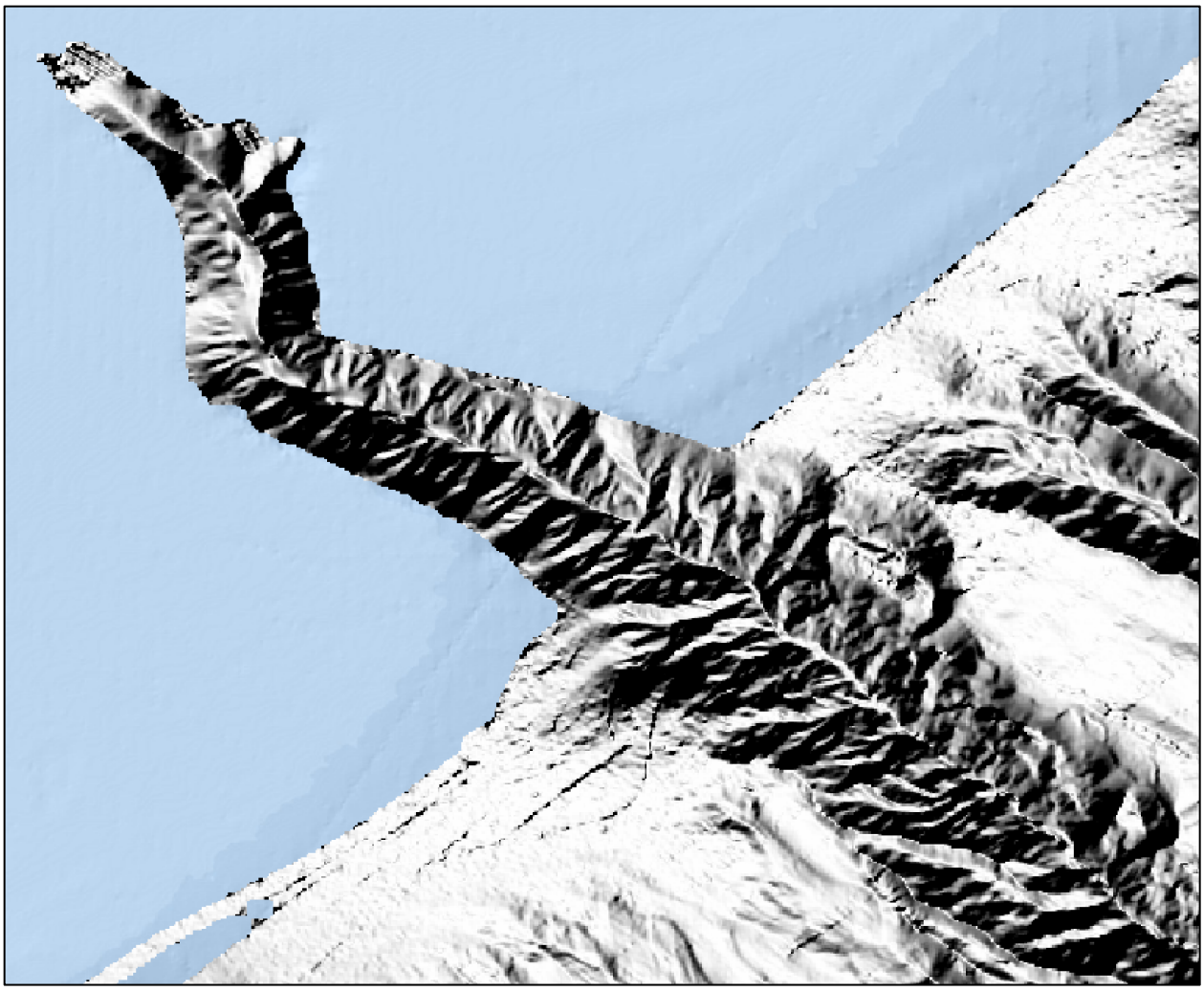

Figure 3.4 Hillshade relief map of the Hudson Canyon region of the survey area.

### 3.3 Bathymetric Position Index

The second phase of the classification process utilized the Benthic Terrain Modeler (BTM) in ESRI ArcGIS (Walbridge et al., 2018). This approach consists of a variety of functions to create grids of seafloor BPI and rugosity. An analysis of the impact of search radius variability on BPI results, analogous to the analysis for the geomorphic approach, was conducted. A change in search radius had a much greater effect on the results with BPI than geomporhons, with most

large seafloor features becoming poorly defined post-classification at search radii greater than 10 cells. Because of this, classification was specified at a 5-cell search radius for consistency with outer search radius used to classify geomorphologic phonotypes. The product was a raster layer that classified the USAM by BPI (Figures 3.5 and 3.6). The BPI values of cells containing points representing seep sites were then sampled to compare the distribution of values between the sites with those of the whole survey area.

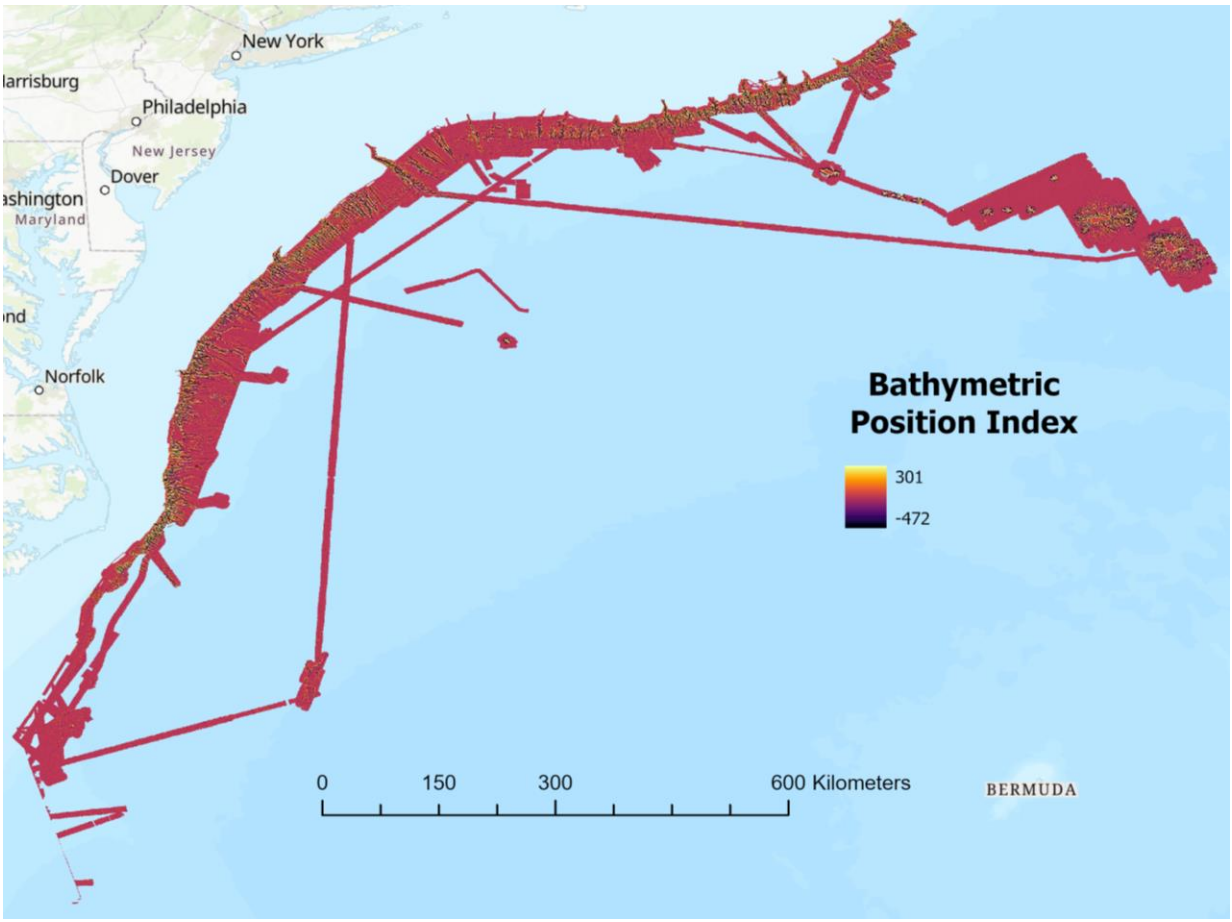


Figure 3.5 Survey area on the United States Atlantic Margin classified by bathymetric position index.

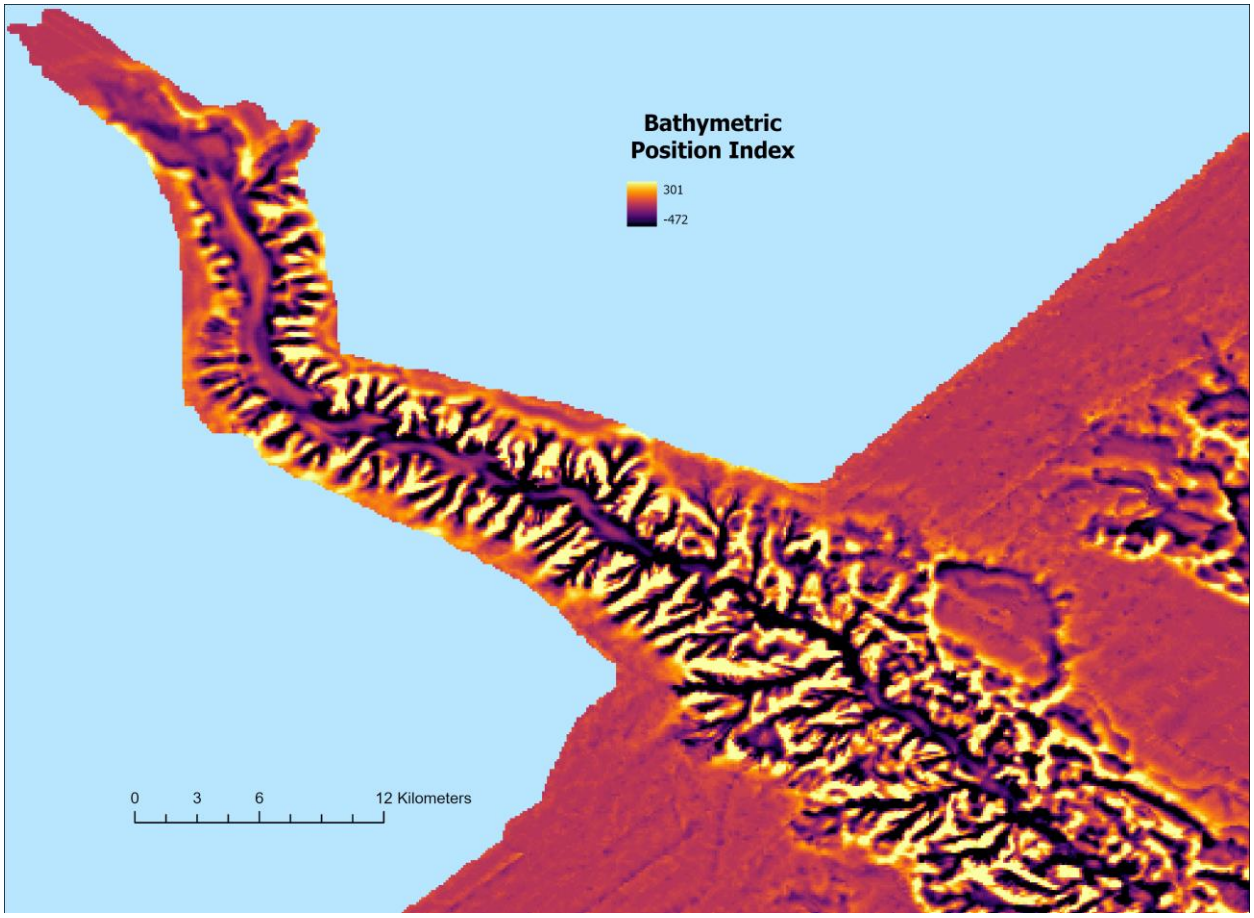


Figure 3.6 Hudson canyon region of the survey area classified by bathymetric position index.

## 3.4 Additional Measures of Seafloor Geomorphology

Once the geomorphon and BPI classifications were complete, the additional variables of slope, rugosity, and aspect were calculated to quantitatively classify seafloor geomorphology at each DEM cell. The functions that classified the bathymetry raster layer according to these variables were also found in the BTM. The BTM calculated slope using 3x3 windows of grid cells, where the center cell and 8 surrounding cells were used to determine the average gradient of both horizontal and vertical directions in the entirety of the raster layer (Figures 3.7 and 3.8). Rugosity was calculated using the Terrain Ruggedness function in the BTM. This function uses

vector analysis to calculate the dispersion of vectors orthogonal to grids cells inside the specified neighborhood (Figures 3.9 and 3.10). Then, aspect was calculated using the function bearing the same name in the BTM, where each cell is classified as one of the four cardinal or four intercardinal directions, with flat areas being given a unique value (Figures 3.11 and 3.12). The slope, rugosity, and aspect values of cells containing points representing seep sites were then sampled to compare the distribution of values between the sites with those of the whole survey area.

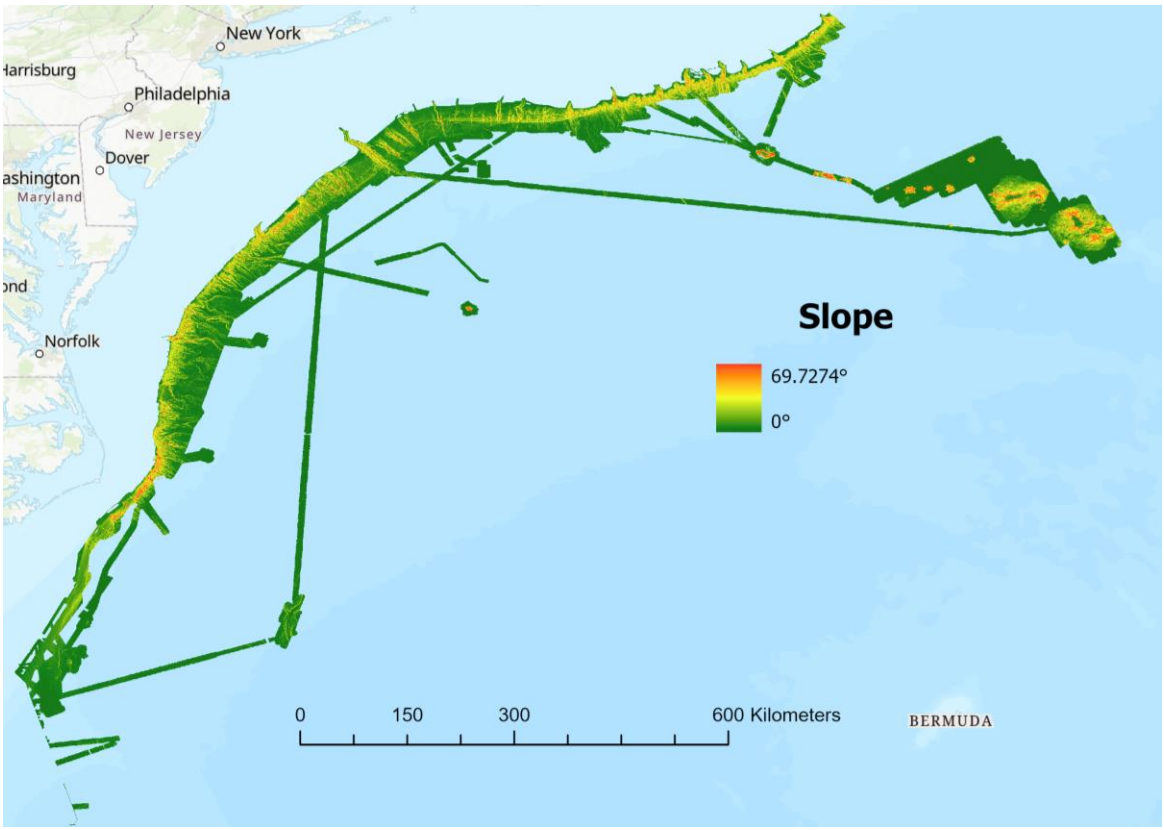


Figure 3.7 Survey area on the United States Atlantic Margin classified by slope.

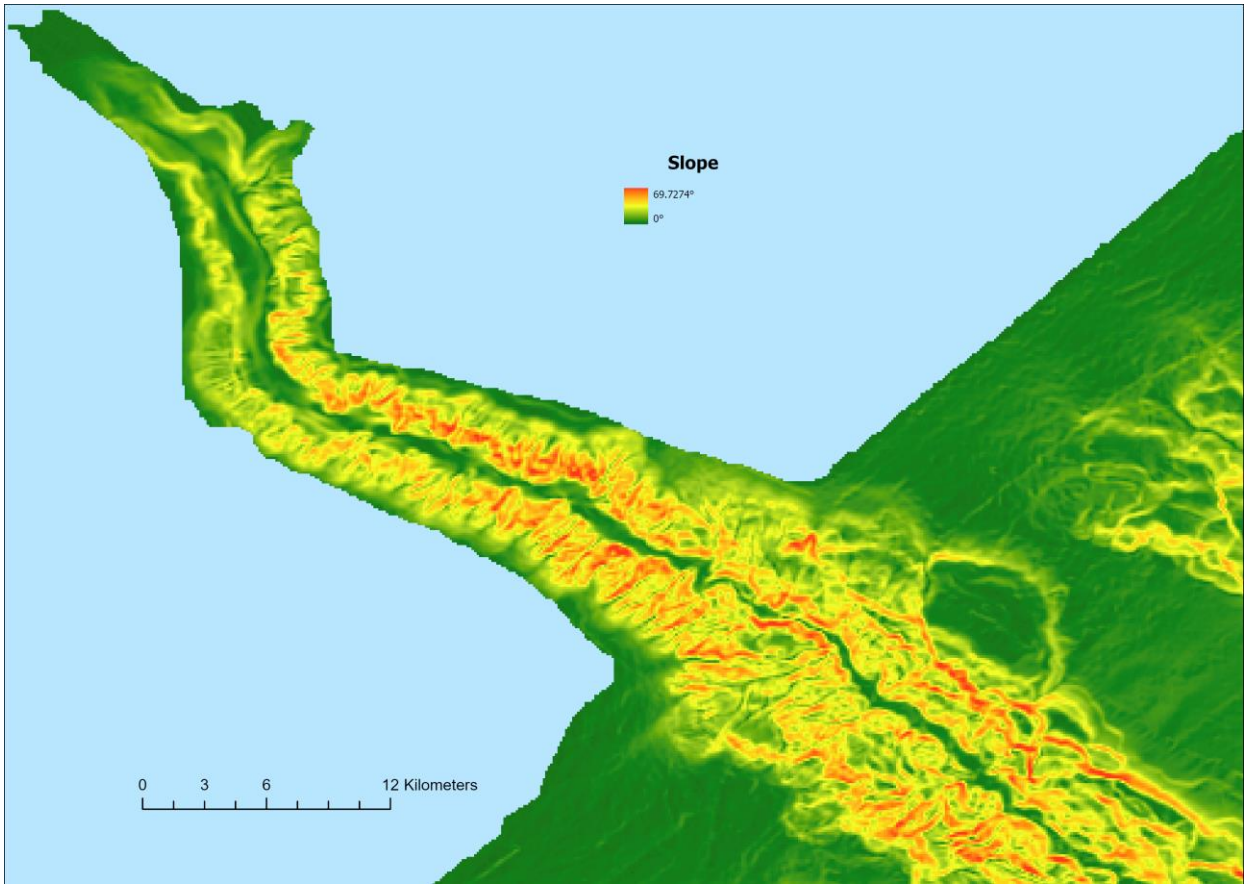


Figure 3.8 Hudson canyon region of the survey area classified by slope.

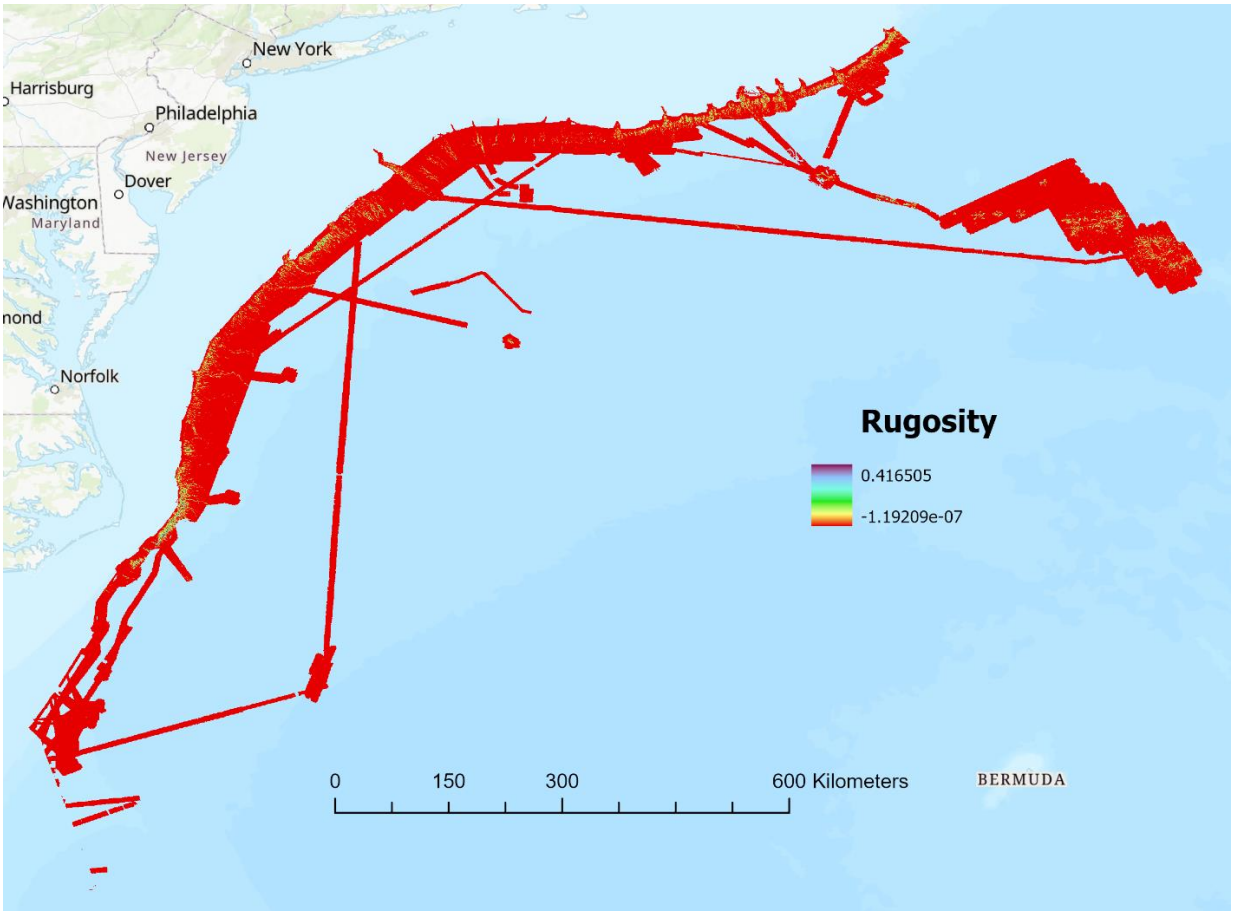


Figure 3.9 Survey area on the United States Atlantic Margin classified by rugosity.

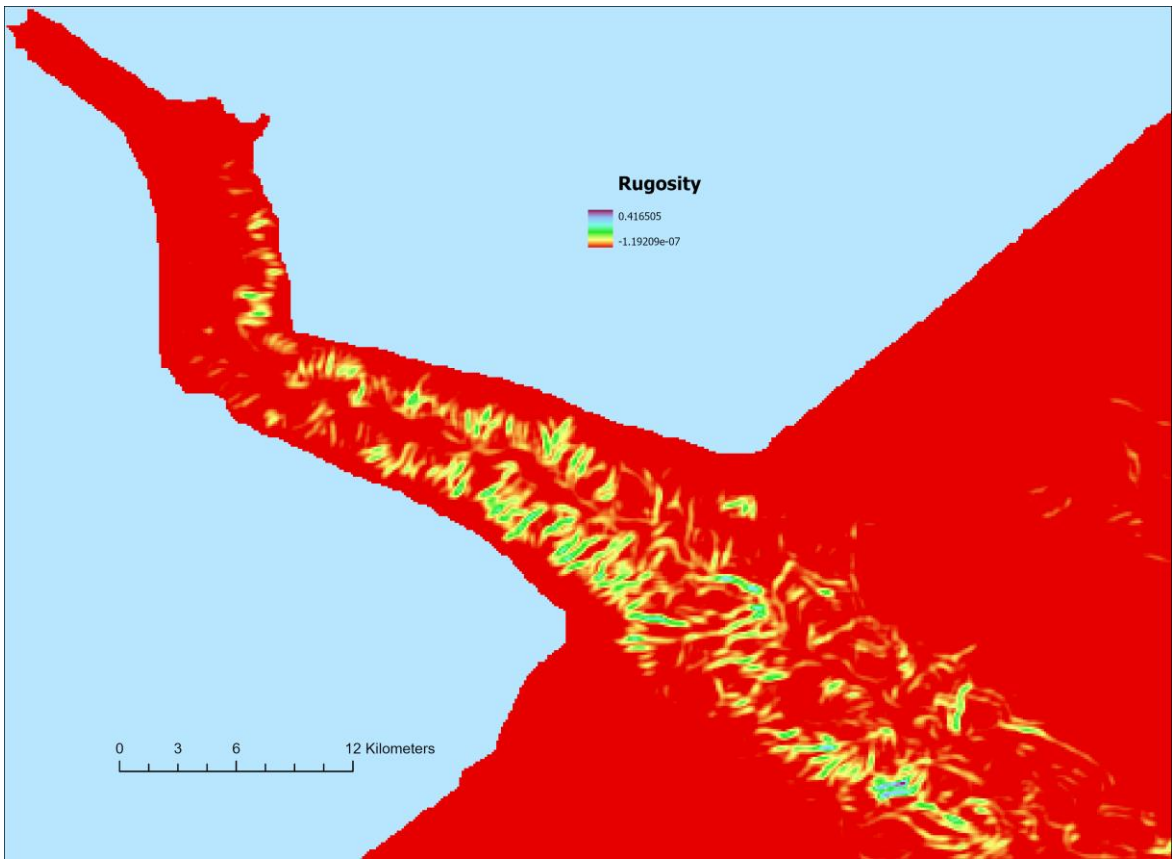


Figure 3.10 Hudson canyon region of the survey area classified by rugosity.

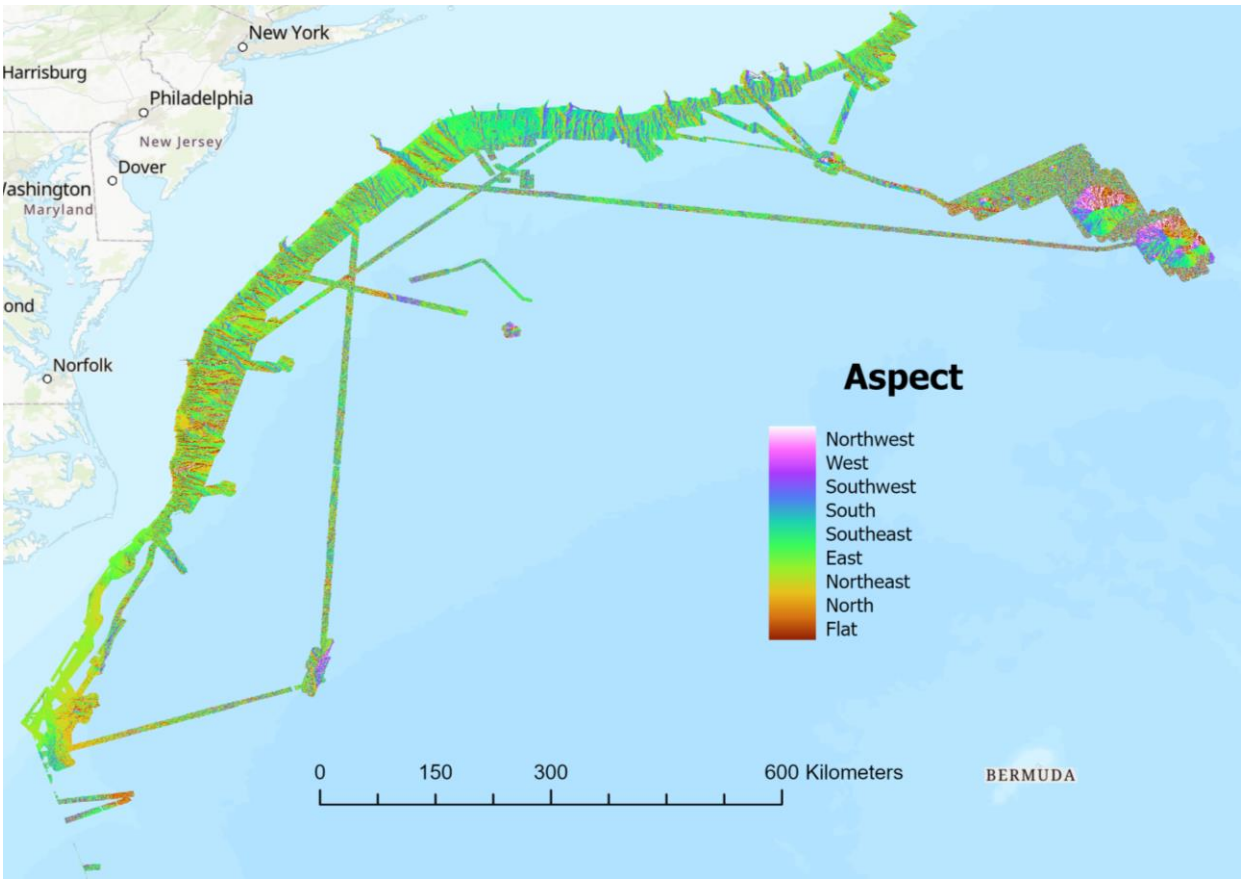


Figure 3.11 Survey area on the United States Atlantic Margin classified by Aspect.

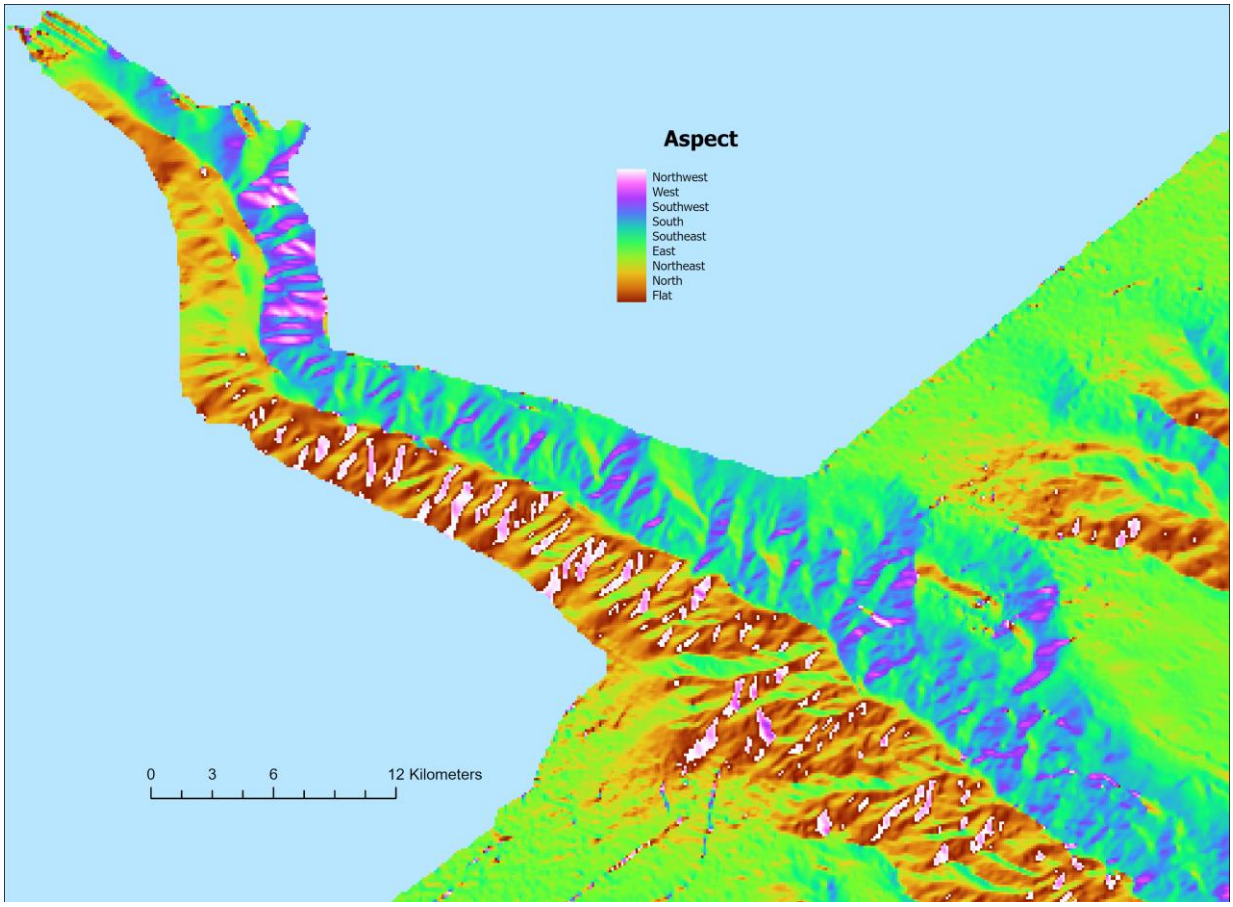


Figure 3.12 Hudson canyon region of the survey area classified by aspect.

## 3.5 Maximum Entropy Modeling

Maximum entropy (maxent) analysis was used to create a prediction model that segmented the survey area according to likelihood of seep presence based on a subset of the previously calculated explanatory variables (geomorphon, BPI, slope, and rugosity) and the locations of determined seep presence. Since geomorphons are classified according to a nominal scale, they were specified as a categorical explanatory variable in the parameters rather than a continuous explanatory variable. To reduce sample bias from isolated clusters of seeps, spatial thinning at 150 meters was incorporated into the parameters. The minimum nearest neighbor

distance of 150 meters was selected to preserve as many points as possible without causing the computation to fail. Next, cross validation of the model was carried out four separate times with three, five, seven, and ten iterations of random resampling used respectively to see if classification results differed by number of resampling attempts. Each iteration of resampling separated the dataset by training and validation using a different portion of the dataset each time. Additional models separating the seep sites by year of identification (2011-2016) were also produced to see how they performed when compared to the model incorporating all seep sites.

# CHAPTER IV

# RESULTS

The frequency distribution of geomorphologic phonotypes at seep sites differs from the frequency distribution of geomorphologic phonotypes across the entire survey area (Figure 4.1) indicating association of seeps with specific geomorphological classes. Fisher's exact test was used to evaluate the statistical significance of these inferred associations (Table 4.2). Results presented in Figure 4.1 and Table 4.1 indicate a statistically significant ($p<0.05$) positive association between seep presence and spur as well as slope geomorphological classes. They also indicate a statistically significant ($p<0.05$) negative association between seep presence and peak, ridge, hollow, valley, and pit geomorphological classes (See Figure 2.6 for illustration of geomorphological classes). Additionally, these results indicate a statistically significant ($p<0.05$) positive association between seep presence and shoulder geomorphological classes for seep locations above the MHSZ. The results further indicate a statistically significant ($p<0.05$) positive association between seep presence and spur as well as ridge geomorphological classes for seep locations within the MHSZ. Finally, the results indicate a statistically significant ($p<0.05$) negative association between seep presence and hollow as well as valley geomorphological classes for seep locations within the MHSZ.

The distribution of BPI at seep sites also differs from the distribution of BPI across the entire survey area (Figure 4.2) suggesting association of seeps with specific BPI ranges. Seep locations exhibit a higher median and mean seafloor BPI relative to the entire survey area. This

relationship also holds for seeps in the portion of the survey area above the MHSZ and is particularly pronounced for the seeps in the portion of the survey area within the MHSZ. Similarly, seep locations exhibit a higher median and mean seafloor slope (Figure 4.3) and rugosity (Figure 4.4) relative to the entire survey area. This relationship also holds for seeps in the portion of the survey area above the MHSZ and is particularly pronounced for the seeps in the portion of the survey area within the MHSZ. Finally, the distribution of seafloor aspect at seep sites also differs slightly from the distribution of aspect across the entire survey area (Figure 4.5). Seep locations exhibit a lower (more easterly) median and mean seafloor aspect (Figure 4.4) and relative to the entire survey area. This relationship also holds for seeps and the portion of the survey area above the MHSZ, but such a relationship is not clearly defined for seeps and the portion of the survey area within the MHSZ due to the multimodality of the seep results. Summary descriptive statistics for these relationships are presented in Table 4.2. Welch's two sample t-test, the Wilcoxon rank sum test, and Watson's $U^2$ test, were used to evaluate the statistical significance of these inferred associations (Table 4.3). Welch's two sample t-test was selected because the sample variances are known to be different and visual evaluation of data distribution (e.g. Figures 4.2 and 4.3) suggest the data are normally distributed and thus a parametric test is applied. However, quantitative testing for normal distribution (Anderson-Darling, Lilliefors, and Kolmogorov-Smirnov) rejects the null hypothesis of normality at a 5% significance level, thus nonparametric significance test (Wilcoxon rank sum test) results were included as well. Watson's $U^2$ test was specifically applied to aspect data due to its circular (azimuthal) nature. All tests consistently indicate the statistical significance ($p<0.05$) of the

Both parametric and non-parametric test results consistently rejected the null hypothesis that morphological observations (BPI, Slope, Rugosity, and Aspect) for seeps and the full survey area are from populations with equal means, with the exception of slope above the MHSZ (table 4.3)

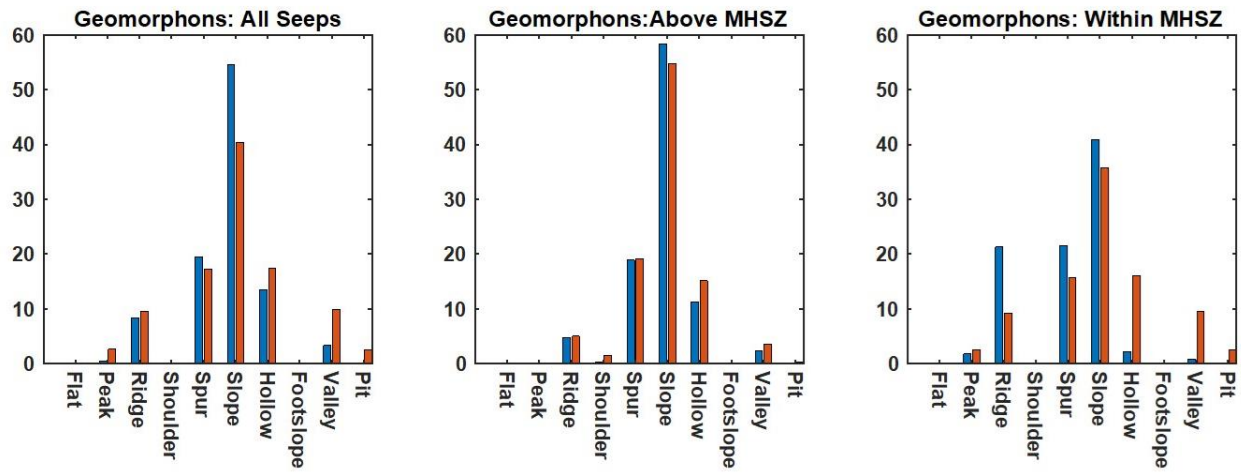


Figure 4.1 Three paired bar charts displaying the difference in distribution of geomorphons amongst seep sites (blue) and the survey area (orange).

Distribution differences are shown for all seeps with the whole survey area, the seep sites and survey area above the MHSZ, and the seep sites and survey area within the MHSZ respectively.

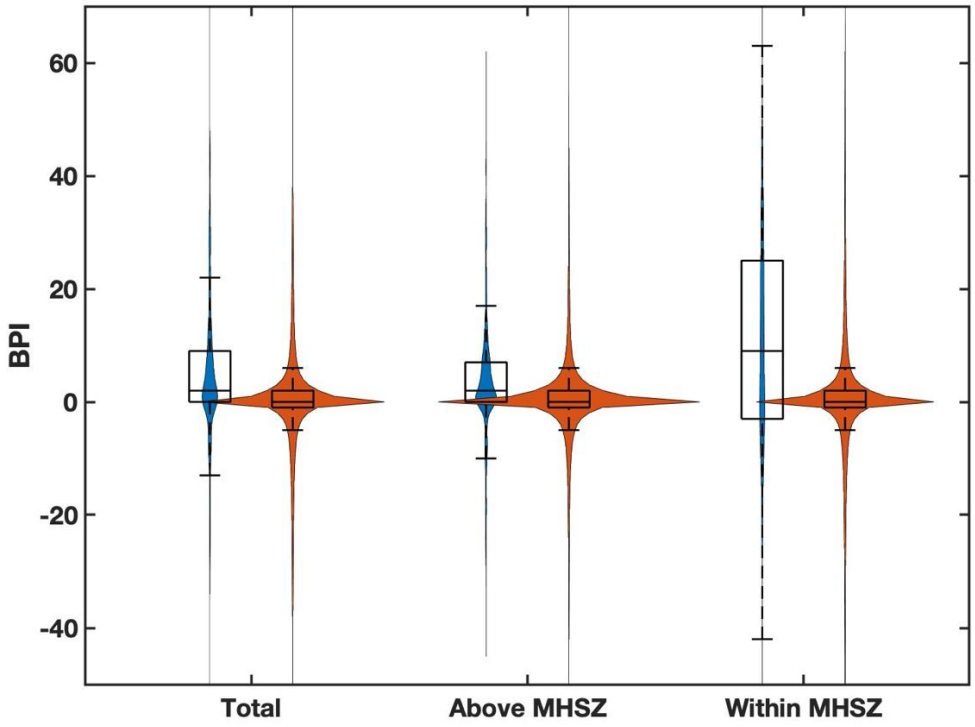


Figure 4.2 Box/violin plot displaying the difference in distribution of BPI values amongst seep sites (blue) and the survey area (orange). Distribution differences are shown for all seeps with the whole survey area, the seep sites and survey area above the MHSZ, and the seep sites and survey area within the MHSZ respectively.

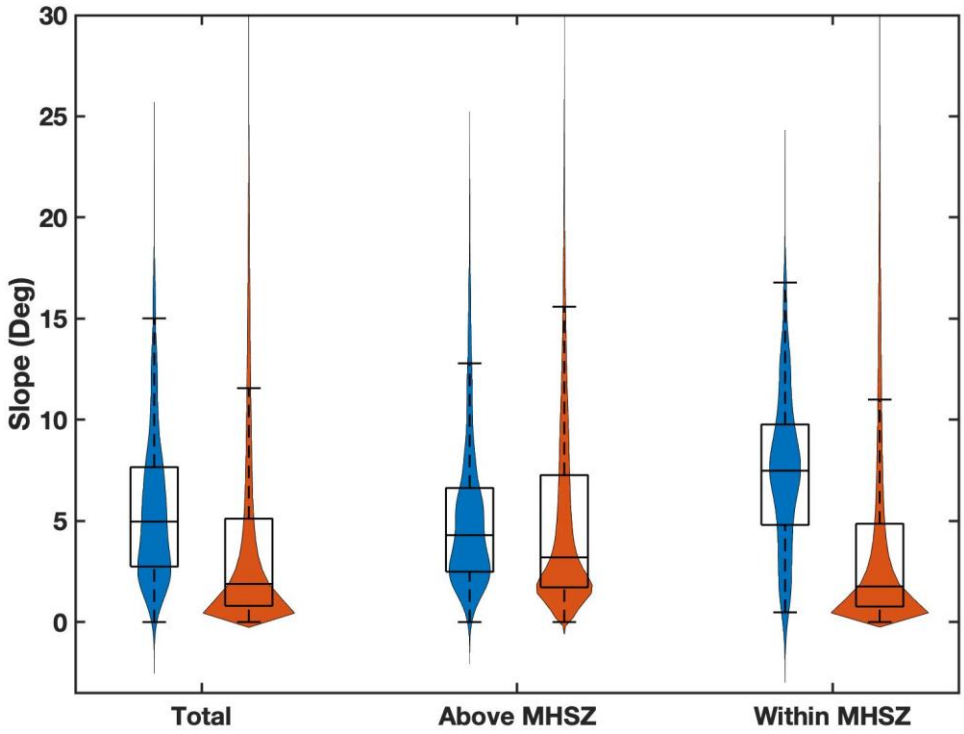


Figure 4.3 Box/violin plot displaying the difference in distribution of slope values amongst seep sites (blue) and the survey area (orange). Distribution differences are shown for all seeps with the whole survey area, the seep sites and survey area above the MHSZ, and the seep sites and survey area within the MHSZ respectively.

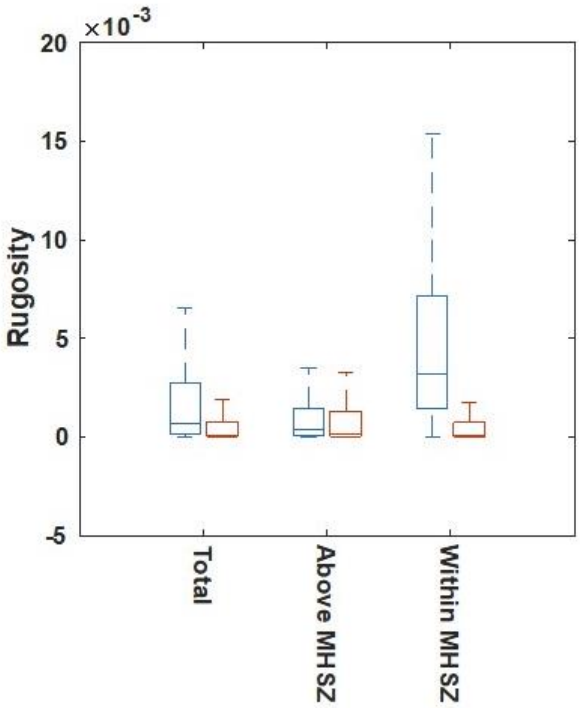


Figure 4.4 Box plot displaying the difference in distribution of rugosity values amongst seep sites (blue) and the survey area (orange). Distribution differences are shown for all seeps with the whole survey area, the seep sites and survey area above the MHSZ, and the seep sites and survey area within the MHSZ respectively.

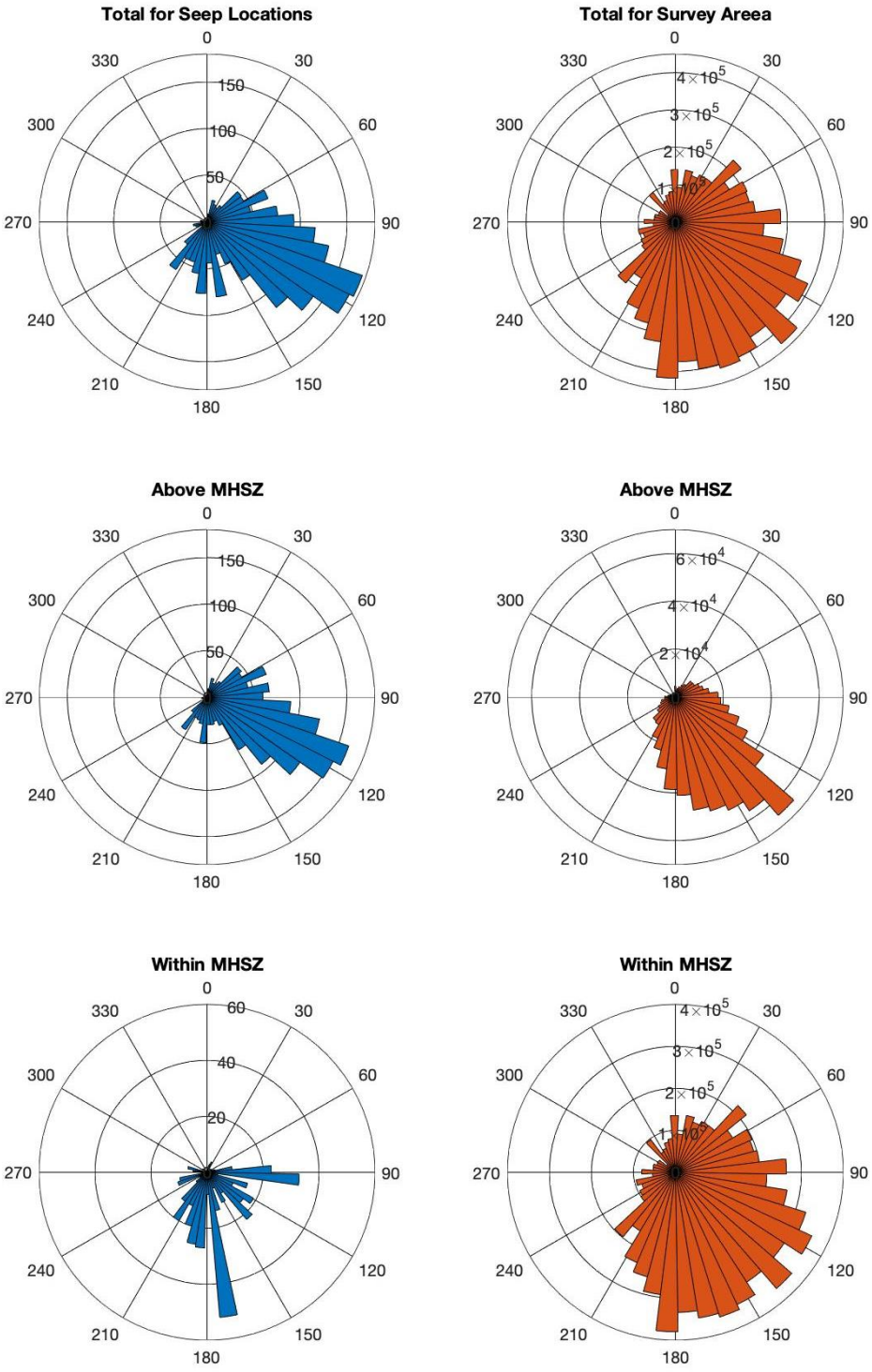


Figure 4.5 Graphic displaying the distribution of aspect values among all seep sites (blue) and the survey area (orange). Distribution differences are shown for all seeps with the whole survey area, the seep sites and survey area above the MHSZ, and the seep sites and area within the MHSZ respectively.

Table 4.1 Significance of association between geomorphons and seep presence. Shaded results are not significant.

| | All Seeps | | | Above MHSZ | | | Within MHSZ | | |
|---|---|---|---|---|---|---|---|---|---|
| | *P-Value* | *Sig* | *Pos/Neg* | *P-Value* | *Sig* | *Pos/Neg* | *P-Value* | *Sig* | *Pos/Neg* |
| **Flat** | 0 | 0 | | 0 | 0 | | 0 | 0 | |
| **Peak** | 2.13E-13 | p<0.05 | Neg | 0.1446 | p>0.05 | | 0.2482 | p>0.05 | |
| **Ridge** | 0.0577 | p>0.05 | | 0.6845 | p>0.05 | | 4.17E-12 | p<0.05 | Pos |
| **Shoulder** | 0.5683 | p>0.05 | | 6.50E-07 | p<0.05 | Neg | 0 | 0 | |
| **Spur** | 0.0109 | p<0.05 | Pos | 0.8217 | p>0.05 | | 0.0156 | p<0.05 | Pos |
| **Slope** | 5.67E-37 | p<0.05 | Pos | 0.0051 | p>0.05 | | 0.4616 | p>0.05 | |
| **Hollow** | 2.62E-06 | p<0.05 | Neg | 0.4577 | p>0.05 | | 3.05E-05 | p<0.05 | Neg |
| **Footslope** | 0.4573 | p>0.05 | | 0.2747 | p>0.05 | | 0 | 0 | |
| **Valley** | 7.15E-29 | p<0.05 | Neg | 0.4505 | p>0.05 | | 2.16E-06 | p<0.05 | Neg |
| **Pit** | 2.24E-21 | p<0.05 | Neg | 0.2 | p>0.05 | | 0 | 0 | |

Table 4.2 Descriptive statistics of seafloor geomorphology results.

| | | Total | | Above MHSZ | | Within MHSZ | |
|---|---|---|---|---|---|---|---|
| | | Survey Area | Seeps | Survey Area | Seeps | Survey Area | Seeps |
| ***n*** | | 9068494 | 1996 | 772023 | 1560 | 8296471 | 436 |
| **BPI** | *mean* | 0.46 | 4.82 | 0.48 | 3.32 | 0.45 | 10.20 |
| | *median* | 0 | 2 | 0 | 2 | 0 | 9 |
| **Slope** | *mean* | 4.04° | 5.72° | 5.05° | 5.21° | 3.95° | 7.57° |
| | *median* | 1.88° | 4.97° | 3.20° | 4.30° | 1.76° | 7.48° |
| **Rugosity** | *mean* | 0.0016 | 0.0022 | 0.00027 | 0.0015 | 0.00027 | 0.0046 |
| | *median* | 0.00012 | 0.00076 | 0.00022 | 0.00045 | 0.00015 | 0.0032 |
| **Aspect** | *mean* | 149.30° | 129.27° | 149.62° | 120.26° | 149.27° | * |
| | *median* | 146.31° | 121.96° | 148.24° | 116.82° | 146.31° | * |

** The distribution of aspect for seeps within the MHSZ is multimodal (Figure 4.5), so mean and median have been omitted due to their limited statistically descriptive value.*

Table 4.3 Parametric (Welch's Two Sample T Test) and nonparametric (Wilcoxon Rank Sum Test) tests showing statistical significance of results from analyses of BPI, Slope, Rugosity, and Aspect. Shaded results are not significant.

| | | **Welch's Two Sample T Test** | | **Wilcoxon Rank Sum Test** | **Median Effect Size** | **Confidence Interval 95%** |
|---|---|---|---|---|---|---|
| | | *T Statistic* | *P Value* | *P Value* | | |
| **BPI** at Seeps vs Full Survey Area | *Total* | -14.59 | 6.7769e-46 (p<0.05) | 5.7466e-92 (p<0.05) | 4.37 | 3.86 - 4.90 |
| | *Above MHSZ* | -10.15 | 1.7334e-23 (p<0.05) | 9.7003e-79 (p<0.05) | 2.84 | 2.40 - 3.28 |
| | *Within MHSZ* | -10.96 | 7.5321e-25 (p<0.05) | 5.7929e-28 (p<0.05) | 9.74 | 8.59 - 10.90 |
| **Slope** at Seeps vs Full Survey Area | *Total* | -19.76 | 1.5370e-79 (p<0.05) | 1.1205e-222 (p<0.05) | 1.68 | 1.46 - 1.91 |
| | *Above MHSZ* | -1.7443 | 0.0813 (p>0.05) | 2.0225e-20 (p<0.05) | 0.16 | -0.07 – 0.39 |
| | *Within MHSZ* | -19.71 | 2.9600e-62 (p<0.05) | 2.5265e-93 (p<0.05) | 3.61 | 3.13 - 4.11 |
| **Rugosity** at Seeps vs Full Survey Area | *Total* | -7.39 | 2.2135e-13 (p<0.05) | 8.2906e-115 (p<0.05) | 0.0006 | 0.0004 - 0.0000 |
| | *Above MHSZ* | -17.35 | 1.2614e-61 (p<0.05) | 8.8253e-14 (p<0.05) | 0.0012 | 0.001 - 0.0015 |
| | *Within MHSZ* | -19.43 | 1.6188e-61 (p<0.05) | 1.6425e-25 (p<0.05) | 0.004 | 0.003 – 0.006 |
| | | | | **Watson's $U^2$ Test** | | |
| | | | | *P Value* | | |
| **Aspect** at Seeps vs Full Survey Area | *Total* | | | 6.9437e-56 (p<0.05) | -20.04 | -23.44 - -16.63 |
| | *Above MHSZ* | | | 6.3854e-99 (p<0.05) | -29.36 | -32.14 - -26.57 |
| | *Within MHSZ* | | | 1.2192e-05 (p<0.05) | 12.09 | 4.65 – 19.53 |

A maximum entropy spatial distribution model was fitted with geomorphon class, BPI, slope, and rugosity as the explanatory variables to generate a predictive distribution map, which indicated the probability of seep presence across the survey area (Figures 4.6-4.9). Cos validation (was used to iteratively validate the model with subsets of validation data that were held out of the training data set. Validation results (Table 4.4) indicate that approximately 81% of the seep

sites were correctly classified, occurring in locations that the model deemed as having a probability of seep presence greater than 50% (Figures 4.10 and 4.11). This result was consistent across 3-fold, 5-fold, 7-fold, and 10-fold cross validation. Additionally, several charts displaying the predictive capacity of each morphological factor used as an explanatory variable were also produced (Figures 4.12-4.16). The geomorphons flat, shoulder, and footslope do not appear on the chart in Figure 4.12 due to spatial thinning eliminating all points with those geomorphic classes. This is due to the defined nearest neighbor distance placing points that were originally found on the edge of the grid outside the bounds of the raster. Analysis of maximum entropy predictive model classification results by year of seep detection show relatively consistent rates of correct seep presence classification (76-86%) and seep presence misclassification (14-24%) with a slight drop off in predictive skill (correct classification = 63% / misclassification = 37%) for seeps observed in 2016.

Maximum entropy spatial distribution model results indicate that the seafloor geomorphons peak, ridge, shoulder, spur, slope, hollow, footslope, valley, and pit contribute to the probability of the presence of seeps (Figure 4.12). The spur and slope geomorphon classes exhibit the greatest contribution to the probability of seep presence (<0.8 probability) with valley and pit classes contributing the least. This result is consistent with association data shown in figure 4.1. Additional results indicate that a positive relationship between BPI value and the probability of seep presences with BPI values greater than 20 being strongly predictive of seep presence (probability > 0.8) (Figure 4.13). Additionally, slope values of approximately 5-20° are strongly predictive of seep presence (probability > 0.8) with that probability of seep presence decreasing rapidly as slope becomes gentler than 5° or steeper than 20° (Figure 4.14). Notably, results indicate that there is no relationship between rugosity and probability of seep presence

indicating the geomorphological characteristic indicated by rugosity (roughness) is not predictive of seep presence (Figure 4.15). Finally, aspect values of approximately 20°-180° are strongly predictive of seep presence (probability > 0.8) with that probability of seep presence decreasing rapidly as aspect becomes less than 20° or greater than 180° (Figure 4.16).

Table 4.4 Maxent predictive model classification results by cross validation resampling method.

| Cross Validation Groups | Area classified as having potential seep presence (Area) (>0.5) | Area classified as having potential seep presence (Percent) (>0.5) | Area classified as having no potential seep presence (Area) (<0.5) | Area classified as having no potential seep presence (Percent) (<0.5) | Seep Presence Correctly Classified (Percent) | Seep Presence Misclassified (Percent) |
|---|---|---|---|---|---|---|
| 3-Fold | 40,670.65 $km^2$ | 45.56% | 48,597.67 $km^2$ | 54.44% | 81.77% | 18.23% |
| 5-Fold | 40,304.65 $km^2$ | 45.15% | 48,963.67 $km^2$ | 54.85% | 81.08% | 18.92% |
| 7-Fold | 39,938.65 $km^2$ | 44.74% | 49,329.67 $km^2$ | 55.26% | 81.41% | 18.59% |
| 10-Fold | 39,983.28 $km^2$ | 44.79% | 49,285.04 $km^2$ | 55.21% | 80.69% | 19.31% |

Table 4.5 Maxent predictive model classification results by year of seep detection. Results acquired using 10-fold cross validation.

| Year | Number of Seep Detections | Area classified as having potential seep presence (>0.5) | Area classified as having potential seep presence (>0.5) | Area classified as having no potential seep presence (<0.5) | Area classified as having no potential seep presence (<0.5) | Seep Presence Correctly Classified | Seep Presence Misclassified |
|---|---|---|---|---|---|---|---|
| 2011 | 47 | 48,785.14 $km^2$ | 54.65% | 40,488.18 $km^2$ | 45.35% | 85.71% | 14.29% |
| 2012 | 545 | 28,735.47 $km^2$ | 32.19% | 60,532.85 $km^2$ | 67.81% | 81.11% | 18.89% |
| 2013 | 307 | 40,965.23 $km^2$ | 45.89% | 48,303.09 $km^2$ | 54.11% | 75.69% | 24.31% |
| 2014 | 672 | 41,616.89 $km^2$ | 46.62% | 47,651.43 $km^2$ | 53.38% | 83.13% | 16.87% |
| 2015 | 192 | 27,664.25 $km^2$ | 30.99% | 61,604.07 $km^2$ | 69.01% | 75.76% | 24.24% |
| 2016 | 233 | 13,167.07 $km^2$ | 14.75% | 76,101.24 $km^2$ | 85.25% | 63.08% | 36.92% |

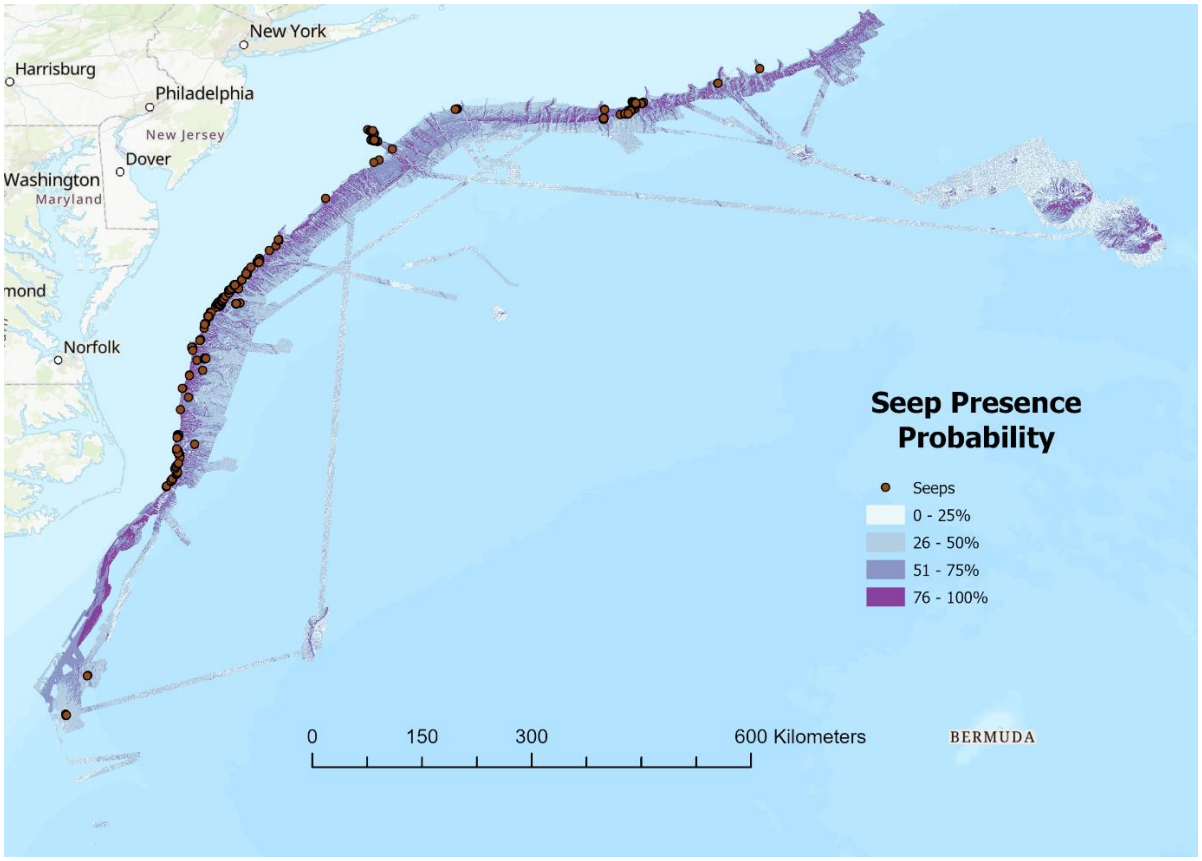


Figure 4.6 Survey area classified by probability of seep presence as calculated by the maximum entropy model. Seep sites are represented by orange points.

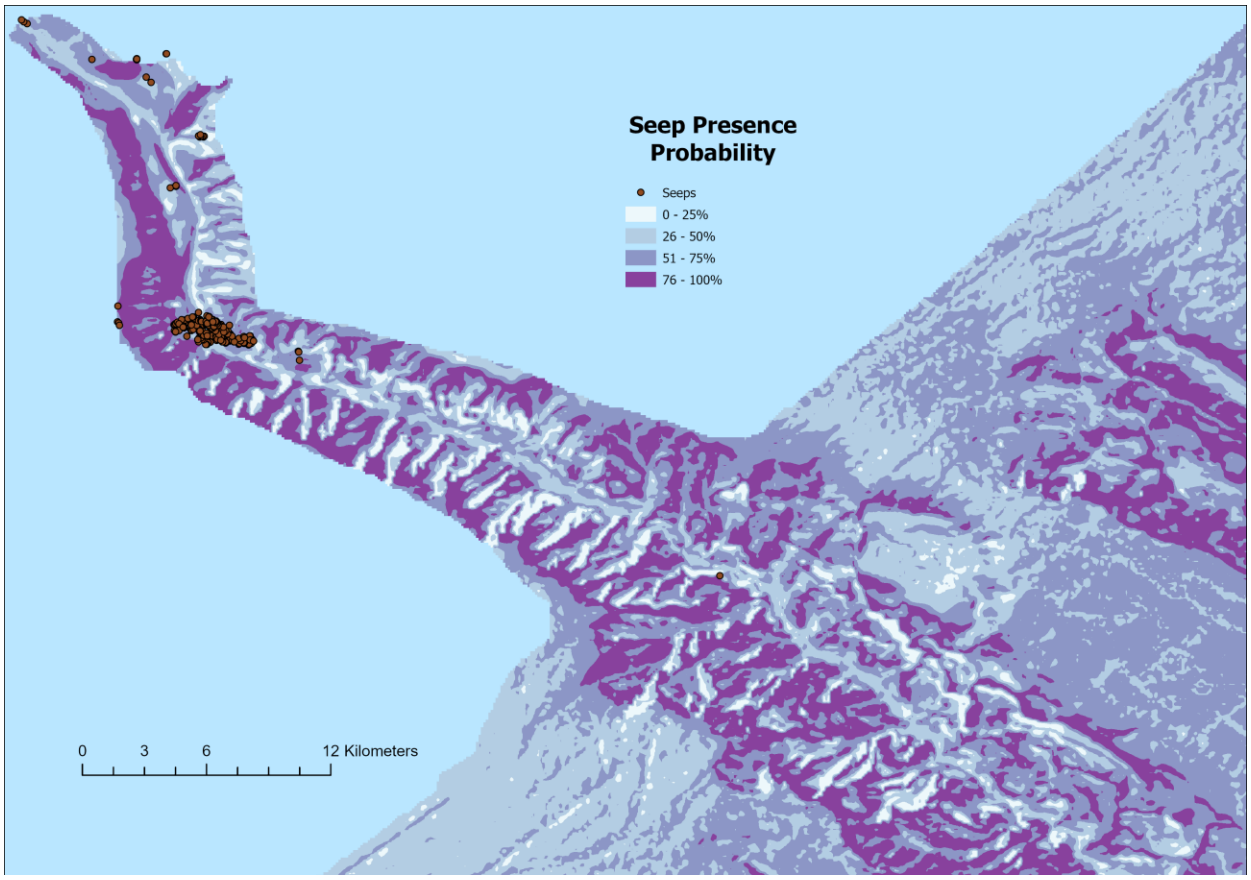


Figure 4.7 Hudson canyon region of the survey area classified by probability of seep presence as calculated by the maximum entropy model. Seep sites are represented by orange points.

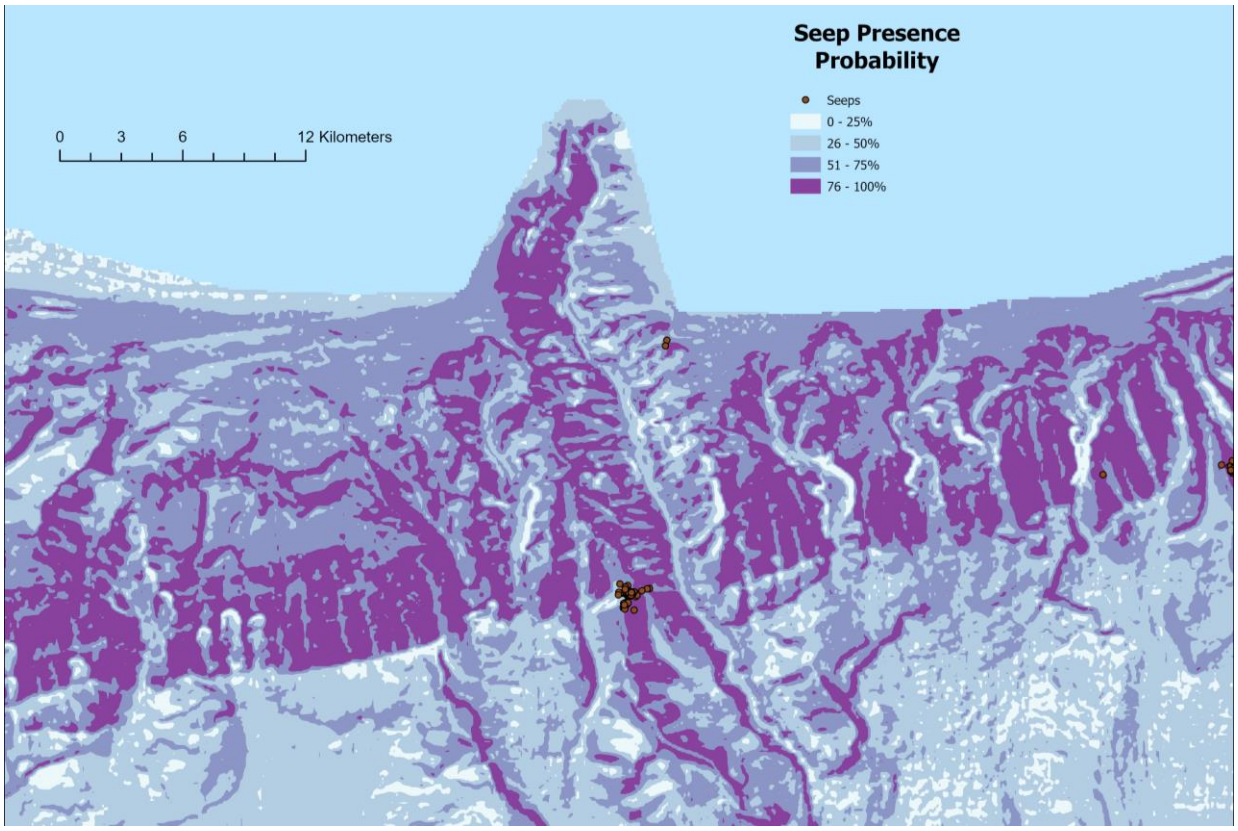


Figure 4.8 Veatch canyon region of the survey area classified by probability of seep presence as calculated by the maximum entropy model. Seep sites are represented by orange points.

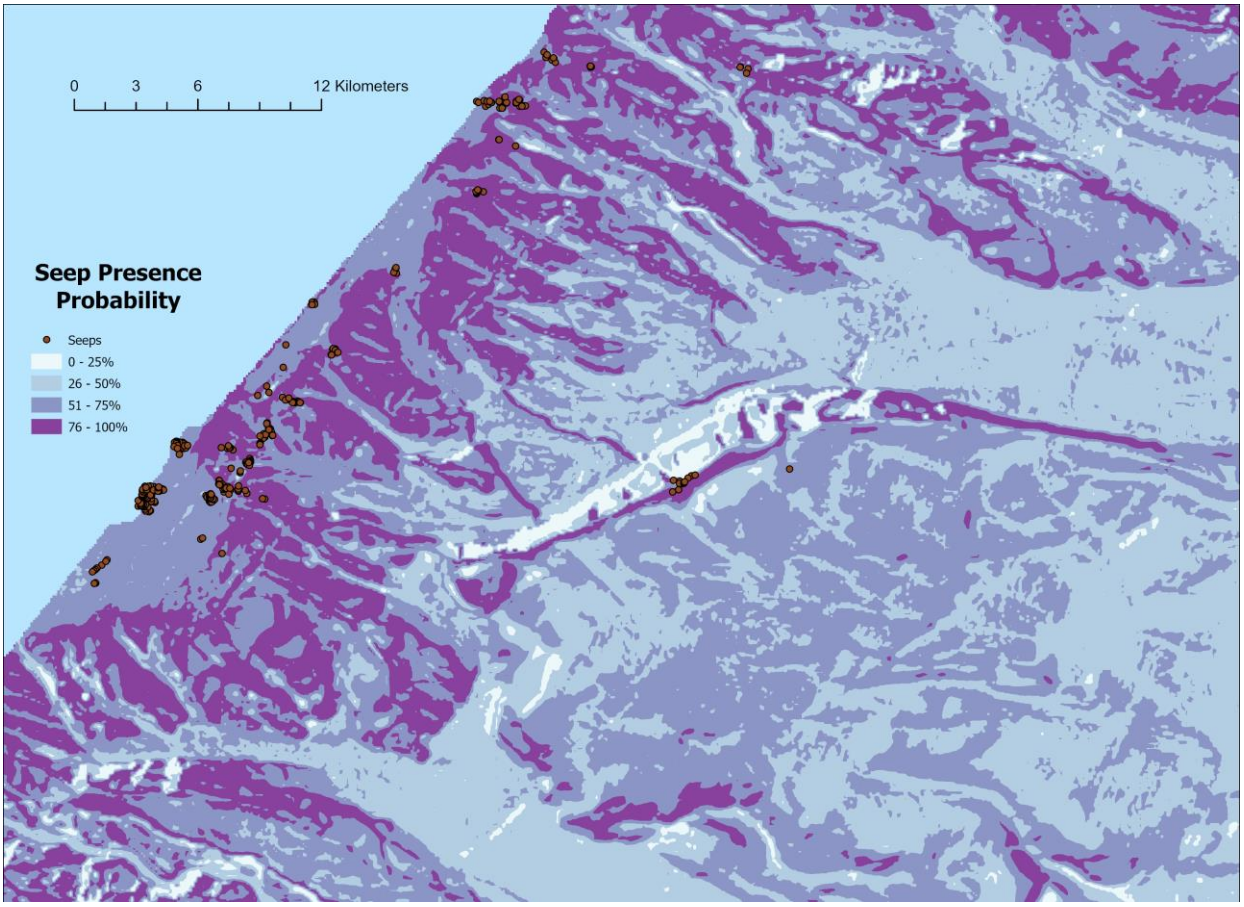


Figure 4.9 Washington canyon region of the survey area classified by probability of seep presence as calculated by the maximum entropy model. Seep sites are represented by orange points.

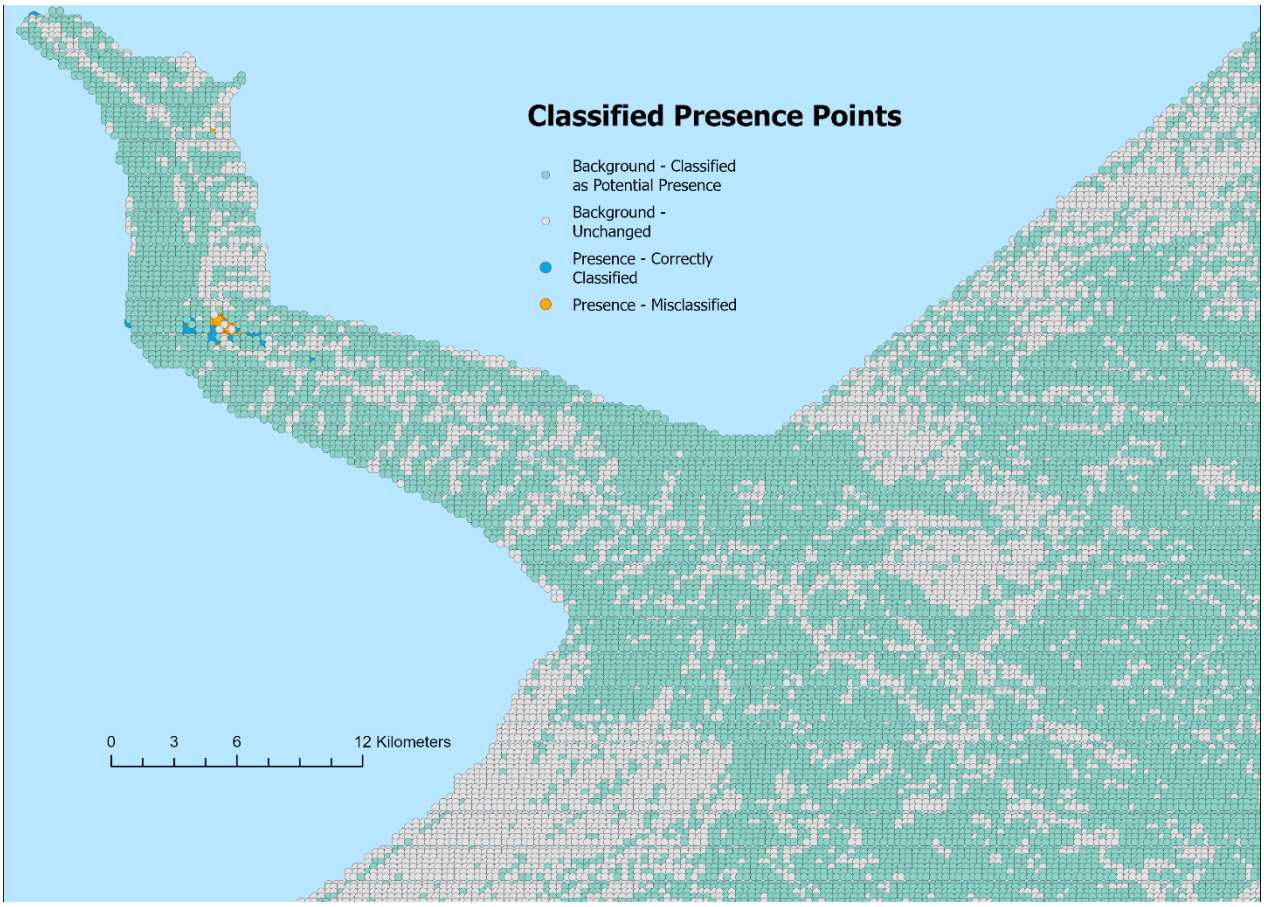


Figure 4.10 Hudson Canyon region of the survey area classified by presence as points. Green represents background points (non-seep points) classified as potential presence. Grey represents points classified as no potential presence. Blue represents points correctly classified as containing a seep. Yellow represents points misclassified as not containing a seep.

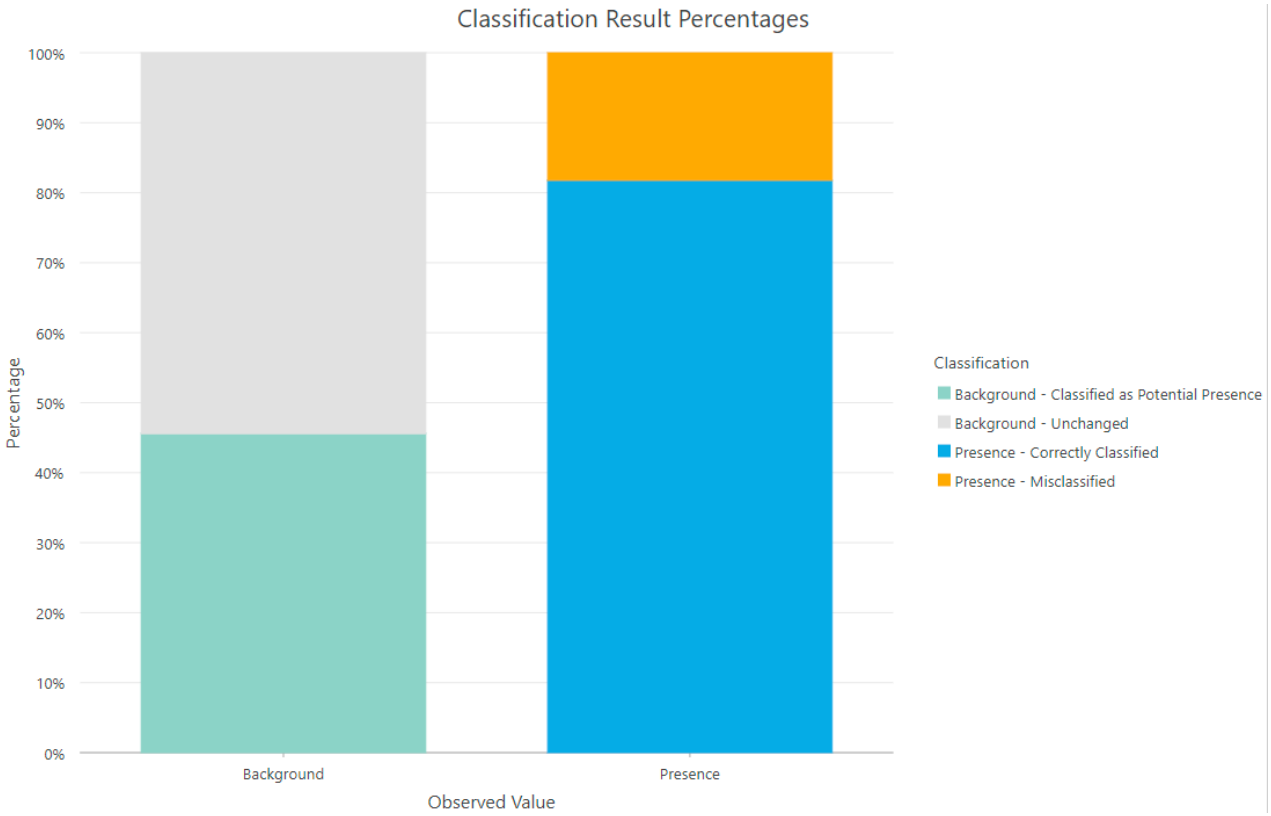


Figure 4.11 Chart showing the distribution of both background points and presence points produced by the model with three iterations of random resampling. Approximately 45.56% of background points are classified as potential presence, while 81.77% of presence points are deemed correctly classified.

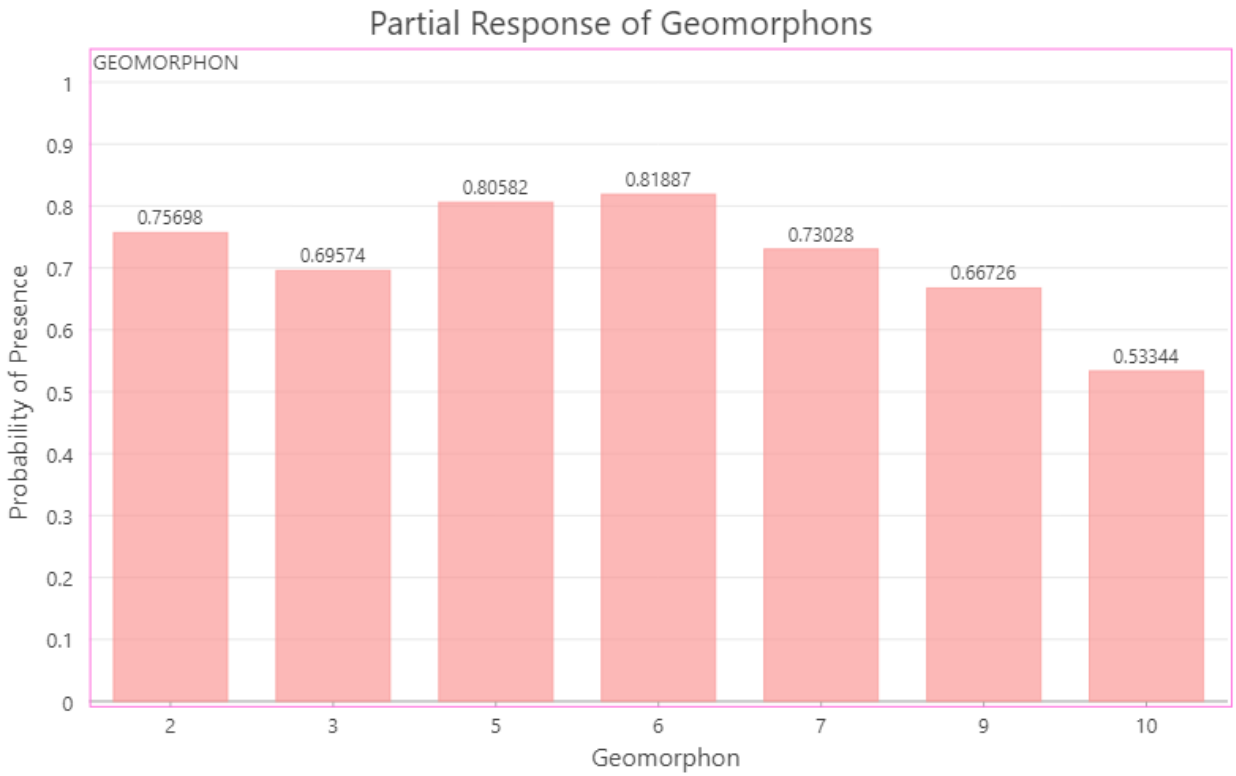


Figure 4.12 Chart showing influence of each geomorphon on seep presence probability. Geomorphon classes shown: (2) peak (3) ridge (4) shoulder (5) spur (6) slope (7) hollow (8) footslope (9) valley (10) pit. See Figure 2.6 for illustration of geomorphological classes.

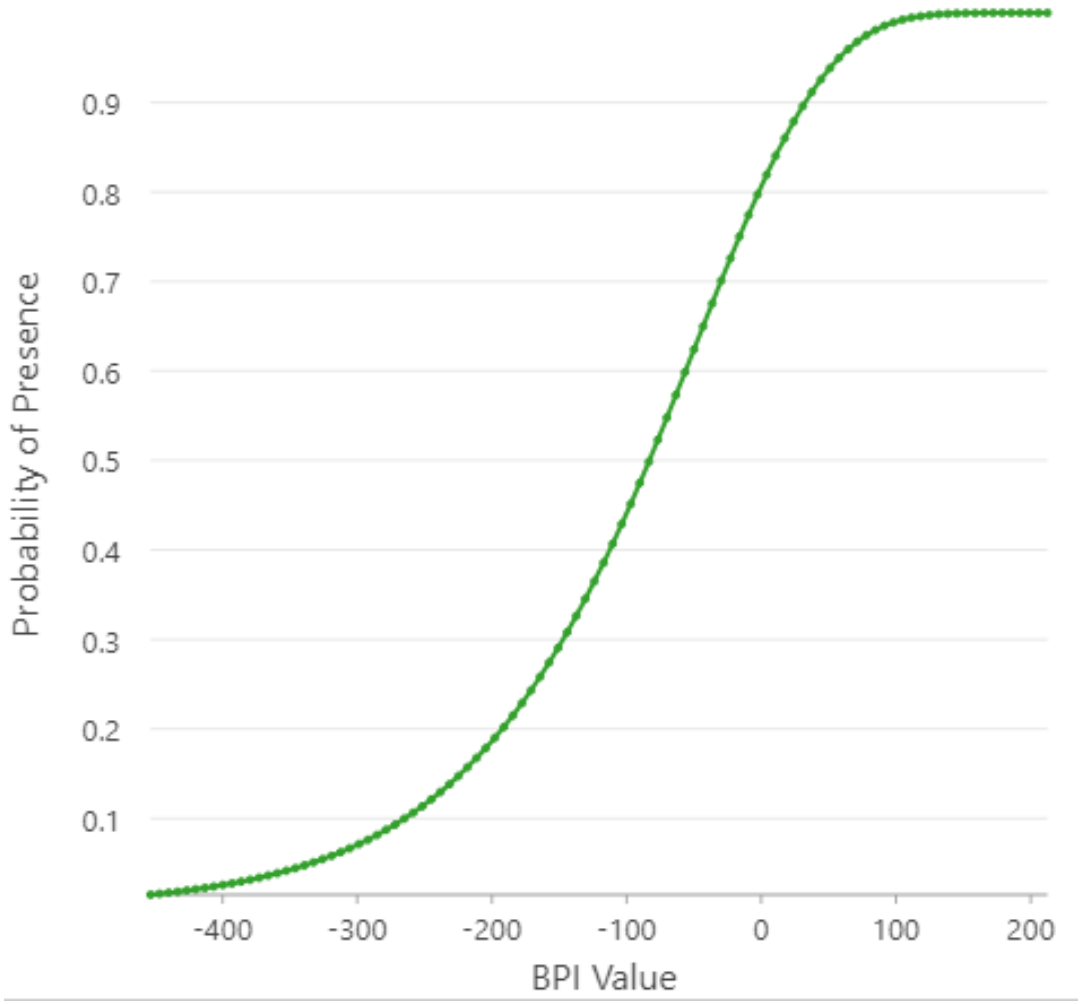


Figure 4.13 Graph showing influence of BPI values on presence probability.

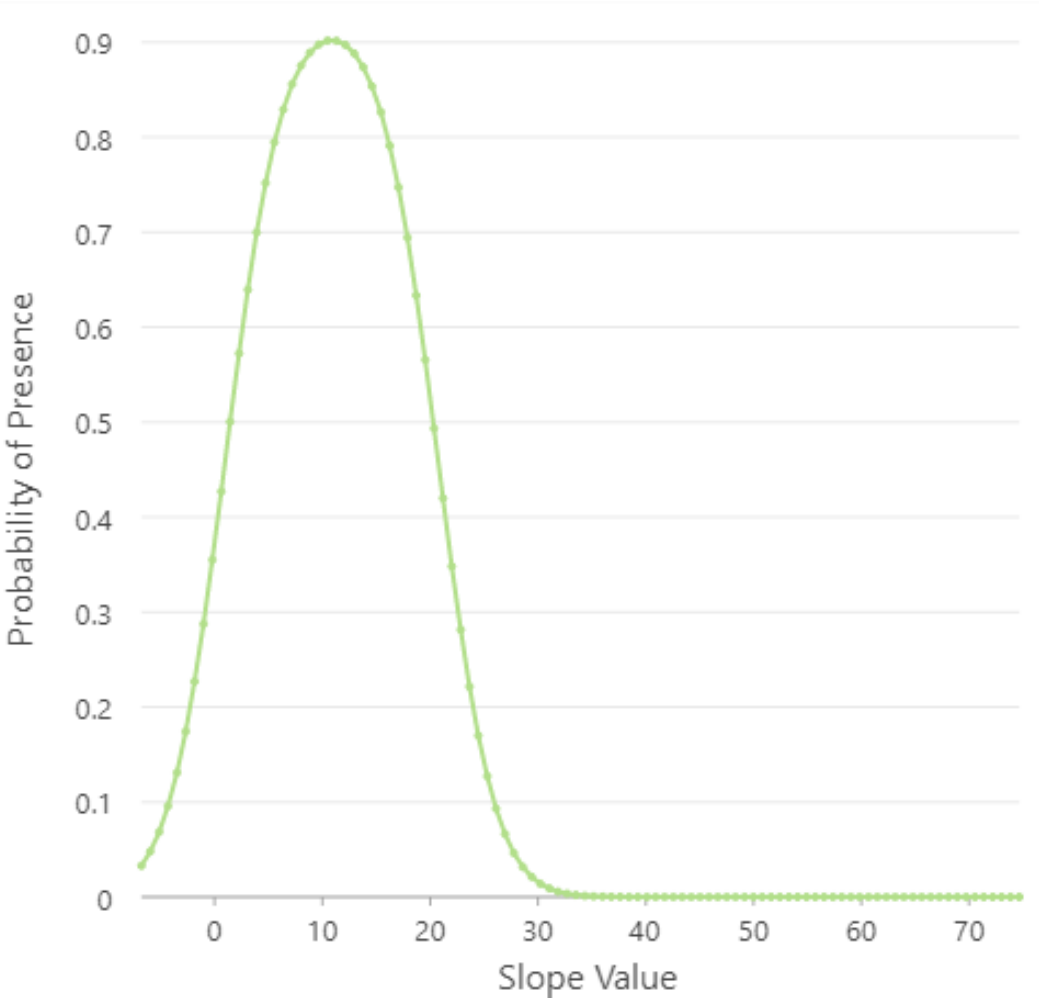


Figure 4.14 Graph showing influence of slope values on presence probability.

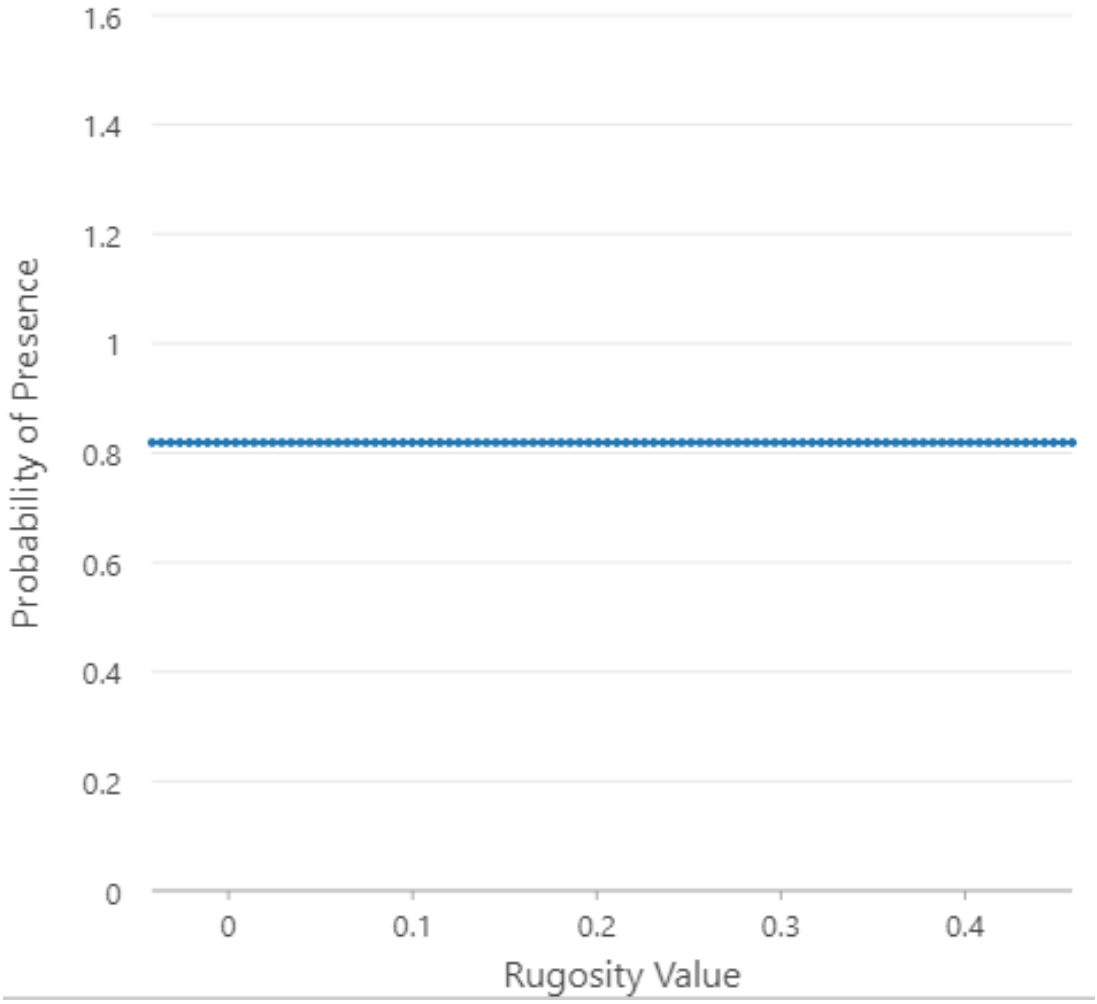


Figure 4.15 Graph showing influence of Rugosity values on presence probability.

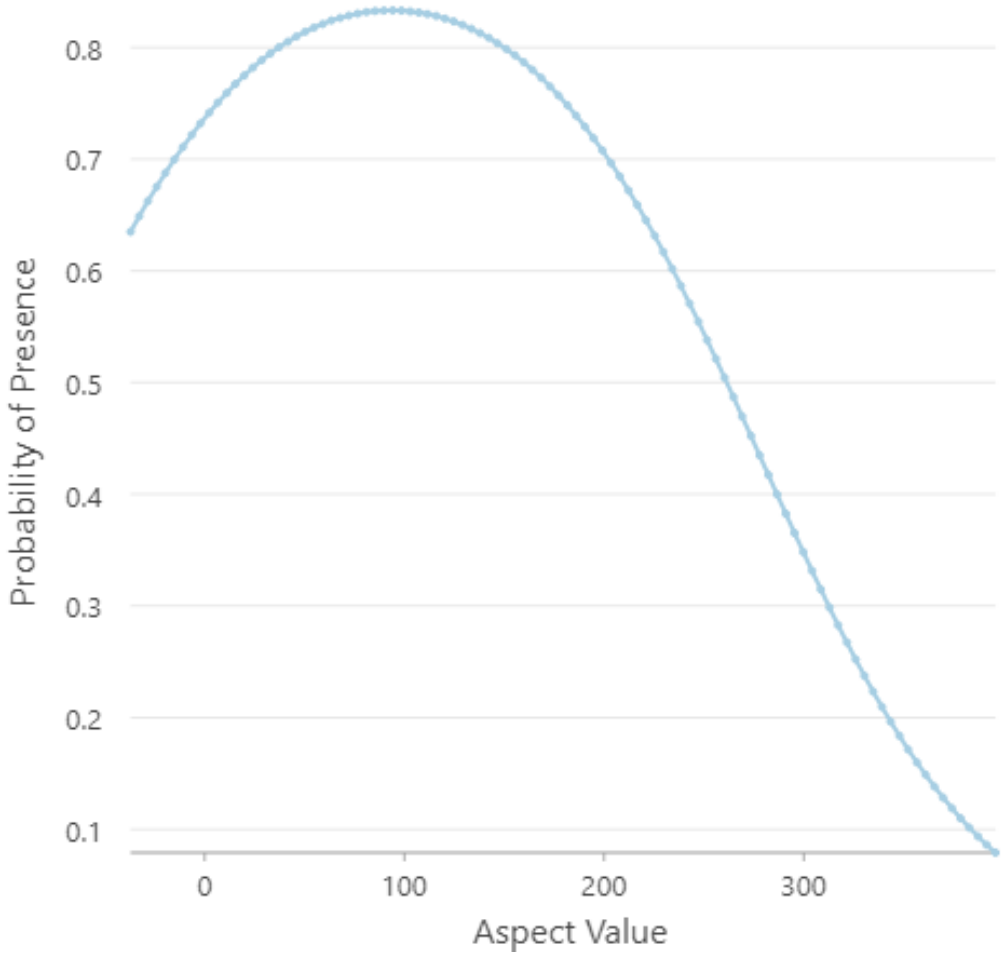


Figure 4.16 Graph showing influence of Aspect values on presence probability.

# CHAPTER V

# DISCUSSION

The overall goal of this research was to evaluate the degree of spatial association between gas seep locations and quantitative measures of seafloor geomorphology. Results indicate that such spatial associations do exist, are statistically significant, and yield insight into the degree to which specific seafloor geomorphological characteristics are associated with seep presence. Additionally, maximum entropy distribution modeling supports the existence of spatial association between seeps and seafloor geomorphological characteristics and quantifies the contribution of specific geomorphological characteristics to the probability of seep presence at a given location. The hypothesis of this thesis is that methane seeps on the USAM have the greatest spatial correlation with bathymetric high points. The presented results strongly support this hypothesis for seep locations within the MHSZ; however, they only moderately support this hypothesis for seep locations above the upper limit of the MHSZ.

Analysis of association between geomorphological phonotype classes and seep location indicate that seep locations above the upper limit of the MHSZ are negatively associated with shoulder geomorphons. This significant ($p<0.05$) negative association between seep presence and shoulder morphology is inconclusive with regard to the hypothesis because a shoulder geomorphological phonotype classification does not represent a discreet bathymetric high or low point. This is also true of the slope, footslope, and flat classes, indicating a shortcoming of the geomorphological phonotype classification approach with regard to evaluating the stated

hypothesis. More conclusive results were generated by analysis of association between geomorphological phonotype classes and seep locations within the MHSZ, which indicate geomorphological classification at seep locations within the MHSZ have a significant ($p<0.05$) positive association with ridge and spur geomorphons as well as a significant ($p<0.05$) negative association with hollow and valley geomorphons. Positive association between seep presence and discrete bathymetric high points (ridge and spur) and negative association between seep presence and discrete bathymetric low points (hollow and valley,) support the hypothesis of this thesis. Collective analysis of all seeps (above and within the MHSZ) indicates significant ($p>0.05$) positive association between seep location and spur geomorphon (bathymetric high) geomorphon as well as significant ($p>0.05$) negative association between seep location and hollow, valley, and pit geomorphons (bathymetric lows), which supports the hypothesis. Additionally, these results indicate significant ($p>0.05$) positive association between seep location and slope geomorphons, which is inconclusive with regard to the hypothesis because a slope does not represent a discreet bathymetric high or low point. Finally, these results indicate significant ($p>0.05$) negative association between seep location and peak geomorphons (bathymetric high), which refutes the hypothesis.

As noted in the background section, positive BPI values indicate that the seafloor at the analyzed location has a higher elevation than the surrounding seafloor and is therefore a bathymetric high point. Negative BPI values indicate that the seafloor at the analyzed location has a lower elevation than the surrounding seafloor and is therefore a bathymetric low point. Because BPI specifically quantifies the degree to which a seafloor location is a bathymetric high or low, it is particularly well suited to directly evaluate the hypothesis of this thesis and overcomes the shortcomings of the geomorphological phonotype approach noted in the

preceding paragraph. Analysis of association between BPI value and seep location indicate that the distribution of BPI at seep sites significantly ($p<0.05$) differs from the distribution of BPI across the entire survey area (Figure 4.2) suggesting association of seeps with specific BPI ranges. Seep locations consistently exhibit a higher median and mean seafloor BPI relative to the entire survey area. This relationship is clear for seeps located above the upper limit of the MHSZ and particularly pronounced for seeps located within the MHSZ. Collectively, the BPI results strongly support the hypothesis of this thesis, demonstrating that seep sites are more frequently associated with bathymetric high points relative to the full survey area.

Analysis of association between seafloor slope and seep location shows that seep locations exhibit a significantly ($p<0.05$) higher median and mean seafloor slope (Figure 4.3) relative to the entire survey area. This relationship is particularly pronounced for the seeps in the portion of the survey area within the MHSZ. This result contributes to the overall goal of this thesis by demonstrating a spatial association between gas seep locations and quantitative measure of seafloor geomorphology (slope). However, it provides no conclusive results with regard to the thesis hypothesis because slope in and of itself is not an indication of a bathymetric high point. Additionally, it seems likely this result reflects the overall morphology of the USAM survey area where the upper limit of the MHSZ, and associated concentration of gas seeps, is on the continental slope. Given the depth of the upper limit of the MHSZ (300-500 m) it seems likely that it will occur on a continental slope within most ocean basins. However, it should be noted that in ocean basins where the upper limit of the MHSZ does not lie on a continental slope, there may not be an association between slope values and seep presence as was demonstrated in this study.

Initial analysis of association between seafloor rugosity and seep location shows that seep locations exhibit a significantly ($p<0.05$) higher median and mean seafloor rugosity (Figure 4.4) relative to the entire survey area. This relationship also holds for seeps in the portion of the survey area above the MHSZ and is particularly pronounced for the seeps in the portion of the survey area within the MHSZ. This is expected, in part, because it is known that seeps have the capacity to generate large seafloor outcrops of authigenic carbonate rock, which create seafloor roughness, which is the morphological characteristic quantified by rugosity. Additionally, seafloor locations with localized bathymetric highs, as hypothesized, inherently are not flat and thus exhibit morphological roughness. However, this relationship should be considered with caution given that subsequent maximum entropy modeling analysis indicates that rugosity has no predictive capacity with regard to the presence of seeps. Accordingly, the rugosity results are indeterminate with regard to the thesis goal and like slope they provide no conclusive results with regard to the thesis hypothesis because rugosity in and of itself is not an indication of a bathymetric high point. A particular challenge of considering using rugosity in this context is the limitations of the resolution of the bathymetric dataset (100 $m^2$) which define the minimum length scales of roughness that can be observed and measured with rugosity. This resolution approaches the upper end of the roughness length scales we would expect seeps to generate through carbonate rock production and thus the capacity of rugosity to quantify roughness at scales relevant to seep processes is limited.

Analysis of association between seafloor aspect and seep location shows that the distribution of seafloor aspect at seep sites also differs slightly from the distribution of aspect across the entire survey area (Figure 4.5). This relationship also holds for seeps and the portion of the survey area above the MHSZ, but such a relationship is not clearly defined for seeps and

the portion of the survey area within the MHSZ due to the multimodality of the seep results. Accordingly, the aspect results are weakly corroborative with regard to the thesis goal and like slope and rugosity they provide no conclusive results with regard to the thesis hypothesis because aspect is not an indication of a bathymetric high point. It seems likely that in a similar fashion to slope, aspect reflects the broadscale southeasterly orientation of the USAM in the study site rather than a key relationship between seafloor orientation and prevailing hydrodynamic conditions unique to seep sites. Thus, in other ocean basins or other parts of the Atlantic basin, it is likely aspect results would reflect local marginal orientation and differ form the result observed here.

Maximum entropy spatial analysis supports the goal of the thesis by clearly indicating, through robust model validation, that quantitative measures of seafloor geomorphology are predictive of the presence of gas seeps (Figure 4.11). Various instances of cross validation using different numbers of random resampling attempts (three, five, seven, and ten) show that validation results are consistent regardless of number of resampling attempts (Table 4.4). Maximum entropy spatial distribution model results indicate that the seafloor geomorphons peak, ridge, shoulder, spur, slope, hollow, footslope, valley, and pit contribute to the probability of the presence of seeps (Figure 4.12). The spur and slope geomorphon classes exhibit the greatest contribution to the probability of seep presence (<0.8 probability) with valley and pit classes contributing the least. This result is consistent with the relative difference in geomorphon distribution between seep location s and the full survey area shown in figure 4.1. Maximum entropy spatial analysis results additionally support the thesis goal by demonstrating that specific ranges of seafloor slope (Figure 4.14) and aspect (Figure 4.16) contribute to the probability of the presence of seeps. Maximum entropy spatial analysis also strongly supports the hypothesis of

this thesis by demonstrating that BPI has a positive relationship with the probability of seep presence (Figure 4.13), This result shows that the seafloor locations most likely to have seeps present are the locations where bathymetric high points have the greatest elevation relative to surrounding seafloor.

Investigation of temporal variability in maxent model results in show that results largely do not differ, except for one instance (Table 4.5). When the model was produced using only seeps detected in 2016, there was a notable drop off in predictive performance. This version of the model only classified 14.75% of the survey area as having potential seep presence. Additionally, it also only classified 63.08% of known seeps correctly. This drop off in performance is likely due to the depth of the seeps recorded in 2016, as most are among the deepest seeps detected. Seep processes at these depths are often driven by salt diapirism, which promotes methane hydrate dissociation through heat conduction within the diapirs. This means that the seeps detected in 2016 are likely being influenced by subsurface geological mechanisms that are not associated with the geomorphological variables included in the model.

It is important to note that predictive skill of the maxent model is limited by a few factors. First, this model has been trained solely on the characteristics of the survey area on the USAM, so its predictive ability may be reduced when applied to different regions, especially those with significant differences in seafloor geomorphology. An example would be the Cascadia margin off the northwestern coast of the United States, which is a tectonically active margin with a more extreme change in gradient and fundamental different geological processes present. Second, the model was based on just five explanatory variables (Geomorphons, BPI, slope, rugosity, and aspect), so other important variables that describe different characteristics of seafloor geomorphology could be missing. Lastly, the model appears to be a better indicator of

where seeps are least likely to be found, as opposed to highlighting where they are most likely to be found. A large portion of the map is classified as exhibiting a 76% or greater likelihood of seep presence, but most of that highlighted region is absent of known seep presence. Collectively, the presented results demonstrate spatial association between gas seep locations and quantitative measures of seafloor geomorphology and support, in part, the hypothesis that that methane seeps on the USAM have the greatest spatial correlation with bathymetric high points. The hypothesis is most directly and clearly supported by the results of BPI analysis.

Based on the presented results, the causative mechanisms responsible for the observed association between seep position and bathymetric high points should be considered. The primary reason association was evaluated separately above and below the upper limit of the MHSZ  in this thesis is because the processes controlling gas release and migration are fundamentally different in each. Above the upper limit of the MHSZ, gas release from hydrate is a result of minute changes in temperature and/or pressure that slowly destabilize methane hydrate at the location where it is most susceptible to dissociation (Ruppel, 2011; Romer et al., 2016). The released buoyant gas migrates upward within sediment pore space until it reaches the seafloor or a low permeability (i.e. confining) sediment layer that impedes its vertical migration. If this occurs, the gas migrates updip along the underside of low permeability layers, it cannot penetrate, until it reaches the seafloor or a vertical pathway to the seafloor such as a fault (Skarke, 2017). Above MHSZ this process can result in slower and more distributed gas release. Within the MHSZ gas release from hydrate is driven by other dissociation processes such as salt diapirisim. These processes can lead to greater rates of discharge and may be more long lived due to their apparent independence from changes in eustatic sea level relative to seeps proximal to the upper limit of hydrate stability. Collectively, this can result in larger carbonate rock

outcrops that create morphological features that are local bathymetric highs within the MHSZ. Field observation of large carbonate rock buildups at seep sites within the MHSZ, and their absence above the upper limit of the MHSZ on the USAM are consistent with this supposition (McVeigh et al, 2018). This may be one reason why the association between gas seep locations and quantitative measures of seafloor geomorphology was observed to be more prominent within the MHSZ.

A second causative mechanism responsible for the observed association between seep position and bathymetric high points could be lateral gas migration of gas under a low permeability confining layer at the seafloor. The transgressive retreat of the eastern North American shoreline since the end of the Pleistocene epoch resulted in current seafloor seep locations becoming more distal from terrestrial terrigenous sediment sources at coastal deltas and estuaries. This transgression could broadly result in an overall fining and increase in clay fraction of seafloor sediment through the Holocene epoch (Diesing, 2020). Collectively this could result in diminished permeability and fluid conductivity of the upper layer of the seafloor (Stranne et al., 2019). A cap of sediment with slightly lower fluid conductivity would serve to trap vertically migrating buoyant gas and transport it laterally through more permeable underlying sediment. This would focus the gas under localized bathymetric highs such as ridges and spurs. Given a lack of observational data, this is highly speculative mechanism. Indeed, processes of erosion and deposition created by downslope mass movement of seafloor sediment through the Holocene would complicate such a conceptual model. Nonetheless, broadscale variability in the conductivity of very shallow seafloor sediment and its role in mediating ga transport pathways should be considered given the associations demonstrated by this thesis.

The results of this thesis could influence future efforts to discover new seep locations, as multibeam sonar surveys could be designed to prioritize coverage of regions that exhibit the morphological characteristics found to be predictive of seep presence. Given that collection of bathymetric and water column data is both temporally and financially costly, continuing to refine our understanding of the controls on seep presence can greatly reduce this cost by reducing the area of expected seep presence and optimizing survey design. A lower cost to surveys can lead to the acquisition of higher quantities of data that will expedite discovery of new seeps and make more efficient the collection of data of broad value to the oceanographic research community.

# CHAPTER VI

# CONCLUSIONS

The aim of this research was to use bathymetric data to determine the degree of spatial association between seep presence and seafloor geomorphology. The results indicate that there is indeed some correlative relationship present between seep site location and bathymetric highs, as hypothesized. Continuous quantitative measures of seafloor geomorphology such as the bathymetric position index, slope, and rugosity differ between those at seep locations and those observed on the entirety of the survey area. Geomorphologic phonotypes, a categorical measure of seafloor geomorphology, also display a difference in distribution when comparing seep locations and the survey area. Additionally, these relationships are more pronounced at locations found within the MHSZ, suggesting different geological mechanisms could be responsible for observed associations at seep sites above the MHSZ and those within the MHSZ. These findings are consistent with previously proposed mechanisms for methane seep emergence, indicating that constraints on subsurface fluid migration pathways are likely a controlling factor. Furthermore, such measures of geomorphology show some predictive potential, allowing for a narrowing of seafloor conditions in which seep presence should be expected.

The practical application of these findings is most relevant in the pursuit of identifying additional regions exhibiting seafloor methane leakage. With a narrowing scope of environments in which seeps can be expected to be found, relevant bathymetric and water column data can be collected in a shorter time frame, allowing for both a deeper understanding of seep processes and

a more rapid acquisition of supplementary seep locations. The model produced by this study could serve as a foundation for improved prediction of seep distribution on other continental margins. However, since the model was built on data collected in a single survey region, its predictive ability could suffer when applied to regions with sufficiently different geomorphology. This could be addressed by conducting similar analyses in other regions and incorporating data from them into the model. The variables used in the model are also constrained by limited data, as there may be additional relevant variables for which data was not available. With these limitations in mind, future research should incorporate a larger set of considered variables as well as surveys conducted in regions with different characteristics, such as those observed above and within the MHSZ. Within the scope of a limited body of knowledge of the controls on seep presence, the methods used here can be expanded and improved upon to provide further insights into the underlying mechanisms controlling the location of methane seeps.

# REFERENCES


Abrams, M. A. (2005). Significance of hydrocarbon seepage relative to petroleum generation and entrapment. *Marine and Petroleum Geology*, *22*(4 SPEC. ISS.). https://doi.org/10.1016/j.marpetgeo.2004.08.003

Andrews, B.D., Chaytor, J.D., ten Brink, U.S., Brothers, D.S., Gardner, J.V., Lobecker, E.A.,and Calder, B.R., 2016, Bathymetric terrain model of the Atlantic margin for marine geological investigations (ver. 2.0, May 2016): U.S. Geological Survey Open-File Report 2012–1266, 12 p., 1 pl., http://dx.doi.org/10.3133/ofr20121266.

Biastoch, A., Treude, T., Rpke, L. H., Riebesell, U., Roth, C., Burwicz, E. B., Park, W., Latif, M., Böning, C. W., Madec, G., & Wallmann, K. (2011). Rising Arctic Ocean temperatures cause gas hydrate destabilization and ocean acidification. *Geophysical Research Letters*, *38*(8). https://doi.org/10.1029/2011GL047222

Chong, Z. R., Pujar, G. A., Yang, M., & Linga, P. (2016). Methane hydrate formation in excess water simulating marine locations and the impact of thermal stimulation on energy recovery. *Applied Energy*, *177*. https://doi.org/10.1016/j.apenergy.2016.05.077

Daigle, H., Cook, A., Fang, Y., Bihani, A., Song, W., & Flemings, P. B. (2020). Gas-Driven Tensile Fracturing in Shallow Marine Sediments. *Journal of Geophysical Research: Solid Earth*, *125*(12). https://doi.org/10.1029/2020JB020835

Davies, R. J., Yang, J., Hobbs, R., & Li, A. (2014). Probable patterns of gas flow and hydrate accretion at the base of the hydrate stability zone. *Geology*, *42*(12). https://doi.org/10.1130/G36047.1

Dean, J. F., Middelburg, J. J., Röckmann, T., Aerts, R., Blauw, L. G., Egger, M., Jetten, M. S. M., de Jong, A. E. E., Meisel, O. H., Rasigraf, O., Slomp, C. P., in't Zandt, M. H., & Dolman, A. J. (2018). Methane Feedbacks to the Global Climate System in a Warmer World. *Reviews of Geophysics*, *56*(1). https://doi.org/10.1002/2017RG000559

Dickens, G. R., O'Neil, J. R., Rea, D. K., & Owen, R. M. (1995). Dissociation of oceanic methane hydrate as a cause of the carbon isotope excursion at the end of the Paleocene. *Paleoceanography*, *10*(6). https://doi.org/10.1029/95PA02087

Diesing, M. (2020). Deep-sea sediments of the global ocean. *Earth System Science Data*, *12*(4). https://doi.org/10.5194/essd-12-3367-2020

Dillon, W. P., Myung, W. L., Fehlhaber, K., & Coleman, D. F. (1993). Gas hydrates on the Atlantic continental margin of the United States - controls on concentration. *US Geological Survey Professional Paper*, *1570*.

Dugan, B., & Sheahan, T. C. (2012). Offshore sediment overpressures of passive margins: Mechanisms, measurement, and models. *Reviews of Geophysics*, *50*(3). https://doi.org/10.1029/2011rg000379

Dugan, B., & Flemings, P. B. (2000). Overpressure and fluid flow in the New Jersey continental, slope: Implications for slope failure and cold seeps. *Science*, *289*(5477). https://doi.org/10.1126/science.289.5477.288

Floodgate, G. D., & Judd, A. G. (1992). The origins of shallow gas. *Continental Shelf Research*, *12*(10). https://doi.org/10.1016/0278-4343(92)90075-U

Fu, X., Waite, W. F., & Ruppel, C. D. (2021). Hydrate Formation on Marine Seep Bubbles and the Implications for Water Column Methane Dissolution. *Journal of Geophysical Research: Oceans*, *126*(9). https://doi.org/10.1029/2021JC017363

Gardner, James V, Mashkoor Malik, and Sharon Walker. "Plume 1400 Meters High Discovered at the Seafloor off the Northern California Margin." Eos, Transactions American Geophysical Union 90, no. 32 (2009): 275. https://doi.org/10.1029/2009EO320003.

Himmler, T., Sahy, D., Martma, T., Bohrmann, G., Plaza-Faverola, A., Bünz, S., Condon, D. J., Knies, J., & Lepland, A. (2019). A 160,000-year-old history of tectonically controlled methane seepage in the Arctic. *Science Advances*, *5*(8). https://doi.org/10.1126/sciadv.aaw1450

Hinrichs, K. U., Hayes, J. M., Bach, W., Spivackl, A. J., Hmelo, L. R., Holm, N. G., Johnson, C. G., & Sylva, S. P. (2006). Biological formation of ethane and propane in the deep marine subsurface. *Proceedings of the National Academy of Sciences of the United States of America*, *103*(40). https://doi.org/10.1073/pnas.0606535103

Jasiewicz, J., & Stepinski, T. F. (2013). Geomorphons-a pattern recognition approach to classification and mapping of landforms. *Geomorphology*, *182*. https://doi.org/10.1016/j.geomorph.2012.11.005

Jaynes, E. T. (1957). Information theory and statistical mechanics. *Physical Review*, *106*(4). https://doi.org/10.1103/PhysRev.106.620

Johnson, H. P., Miller, U. K., Salmi, M. S., & Solomon, E. A. (2015). Analysis of bubble plume distributions to evaluate methane hydrate decomposition on the continental slope. *Geochemistry, Geophysics, Geosystems*, *16*(11). https://doi.org/10.1002/2015GC005955

Joung, Dongjoo, Carolyn Ruppel, John Southon, Thomas S Weber, and John D Kessler. "Negligible Atmospheric Release of Methane from Decomposing Hydrates in Mid-Latitude Oceans," 2022. https://doi.org/10.1038/s41561-022-01044-8.

Joye, S. B. (2020). The Geology and Biogeochemistry of Hydrocarbon Seeps. In *Annual Review of Earth and Planetary Sciences* (Vol. 48). https://doi.org/10.1146/annurev-earth-063016-020052

Judd, A. G. (2003). The global importance and context of methane escape from the seabed. *Geo-Marine Letters*, *23*(3–4). https://doi.org/10.1007/s00367-003-0136-z

Katz, M. E., Pak, D. K., Dickens, G. R., & Miller, K. G. (1999). The source and fate of massive carbon input during the latest paleocene thermal maximum. In *Science* (Vol. 286, Issue 5444). https://doi.org/10.1126/science.286.5444.1531

Kessler, J. D., Valentine, D. L., Redmond, M. C., Du, M., Chan, E. W., Mendes, S. D., Quiroz, E. W., Villanueva, C. J., Shusta, S. S., Werra, L. M., Yvon-Lewis, S. A., & Weber, T. C. (2011). A persistent oxygen anomaly reveals the fate of spilled methane in the deep Gulf of Mexico. *Science*, *331*(6015). https://doi.org/10.1126/science.1199697

Klauda, J. B., & Sandler, S. I. (2005). Global distribution of methane hydrate in ocean sediment. *Energy and Fuels*, *19*(2). https://doi.org/10.1021/ef049798o

Levin, L. A., Baco, A. R., Bowden, D. A., Colaco, A., Cordes, E. E., Cunha, M. R., Demopoulos, A. W. J., Gobin, J., Grupe, B. M., Le, J., Metaxas, A., Netburn, A. N., Rouse, G. W., Thurber, A. R., Tunnicliffe, V., van Dover, C. L., Vanreusel, A., & Watling, L. (2016). Hydrothermal vents and methane seeps: Rethinking the sphere of influence. *Frontiers in Marine Science*, *3*(MAY). https://doi.org/10.3389/fmars.2016.00072

Lurton, X., & Cuschieri, J. M. (2011). An Introduction to Underwater Acoustics—Principles and Applications, (Second Edition). *Noise Control Engineering Journal*, *59*(1). https://doi.org/10.3397/1.3525563

Merle, S. G., Embley, R. W., Johnson, H. P., Lau, T.-K., Phrampus, B. J., Raineault, N. A., & Gee, L. J. (2021). Distribution of Methane Plumes on Cascadia Margin and Implications for the Landward Limit of Methane Hydrate Stability. *Frontiers in Earth Science*, *9*. https://doi.org/10.3389/feart.2021.531714

Naehr, T. H., Eichhubl, P., Orphan, V. J., Hovland, M., Paull, C. K., Ussler, W., Lorenson, T. D., & Greene, H. G. (2007). Authigenic carbonate formation at hydrocarbon seeps in continental margin sediments: A comparative study. *Deep-Sea Research Part II: Topical Studies in Oceanography*, *54*(11–13). https://doi.org/10.1016/j.dsr2.2007.04.010

Phillips, S. J., Anderson, R. P., & Schapire, R. E. (2006). Maximum entropy modeling of species geographic distributions. *Ecological Modelling*, *190*(3–4). https://doi.org/10.1016/j.ecolmodel.2005.03.026

Phrampus, B. J., Lee, T. R., & Wood, W. T. (2020). A Global Probabilistic Prediction of Cold Seeps and Associated SEAfloor FLuid ExpulsionAnomalies (SEAFLEAs). *Geochemistry, Geophysics, Geosystems*, *21*(1). https://doi.org/10.1029/2019GC008747

Prouty, N. G., Sahy, D., Ruppel, C. D., Roark, E. B., Condon, D., Brooke, S., Ross, S. W., & Demopoulos, A. W. J. (2016). Insights into methane dynamics from analysis of authigenic carbonates and chemosynthetic mussels at newly-discovered Atlantic Margin seeps. *Earth and Planetary Science Letters*, *449*. https://doi.org/10.1016/j.epsl.2016.05.023

Riboulot, V., Ker, S., Sultan, N., Thomas, Y., Marsset, B., Scalabrin, C., Ruffine, L., Boulart, C., & Ion, G. (2018). Freshwater lake to salt-water sea causing widespread hydrate dissociation in the Black Sea. *Nature Communications*, *9*(1). https://doi.org/10.1038/s41467-017-02271-z

Römer, M., Riedel, M., Scherwath, M., Heesemann, M., & Spence, G. D. (2016). Tidally controlled gas bubble emissions: A comprehensive study using long-term monitoring data from the NEPTUNE cabled observatory offshore Vancouver Island. *Geochemistry, Geophysics, Geosystems*, *17*(9). https://doi.org/10.1002/2016GC006528

Ruppel, C. D., & Kessler, J. D. (2017). The interaction of climate change and methane hydrates. In *Reviews of Geophysics* (Vol. 55, Issue 1). https://doi.org/10.1002/2016RG000534

Ruppel, C. D. (2011). Methane Hydrates and Contemporary Climate Change. *Nature Education Knowledge*, *3*(10).

Shindell, D. T., Faluvegi, G., Koch, D. M., Schmidt, G. A., Linger, N., & Bauer, S. E. (2009). Improved attribution of climate forcing to emissions. *Science*, *326*(5953). https://doi.org/10.1126/science.1174760

Skarke, A., Ruppel, C., Kodis, M., Brothers, D., & Lobecker, E. (2014). Widespread methane leakage from the sea floor on the northern US Atlantic margin. *Nature Geoscience*, *7*(9). https://doi.org/10.1038/ngeo2232

Skarke, A (2017), High-Resolution Seafloor Mapping at a Deep-Sea Methane Seep Field with an Autonomous Underwater Vehicle, Abstract OS41A-1379 presented at 2017 Fall Meeting, American Geophysical Union, New Orleans, LA., 11-15 Dec.

Stepinski, T. F., & Jasiewicz, J. (2011). Geomorphons—A New Approach to Classification of Landforms. *Proceedings of Geomorphometry 2011, September 7-9, 2011, Redlands, CA*.

Stranne, C., O'Regan, M., Jakobsson, M., Brüchert, V., & Ketzer, M. (2019). Can anaerobic oxidation of methane prevent seafloor gas escape in a warming climate? *Solid Earth*, *10*(5). https://doi.org/10.5194/se-10-1541-2019

Turner, P. J., Ball, B., Diana, Z., Fariñas-Bermejo, A., Grace, I., McVeigh, D., Powers, M. M., van Audenhaege, L., Maslakova, S., Young, C. M., & van Dover, C. L. (2020). Methane Seeps on the US Atlantic Margin and Their Potential Importance to Populations of the Commercially Valuable Deep-Sea Red Crab, Chaceon quinquedens. *Frontiers in Marine Science*, *7*. https://doi.org/10.3389/fmars.2020.00075

Valentine, D. L., Blanton, D. C., Reeburgh, W. S., & Kastner, M. (2001). Water column methane oxidation adjacent to an area of active hydrate dissociation, Eel River Basin. *Geochimica et Cosmochimica Acta*, *65*(16). https://doi.org/10.1016/S0016-7037(01)00625-1

Walbridge, S., Slocum, N., Pobuda, M., & Wright, D. J. (2018). Unified geomorphological analysis workflows with benthic terrain modeler. *Geosciences (Switzerland)*, *8*(3). https://doi.org/10.3390/geosciences8030094

Weber, Thomas C., Larry Mayer, Kevin Jerram, Jonathan Beaudoin, Yuri Rzhanov, and Dave Lovalvo. "Acoustic Estimates Ofmethane Gas Flux Fromthe Seabed in a 6000 Km2 Region in the Northern Gulf of Mexico." American Geophysical Union, 2014, 1911–25. https://doi.org/10.1002/2014GC005271.

Weiss, A. D. 2001. Topographic Positions and Landforms Analysis (Conference Poster). ESRI International User Conference. San Diego, CA, July 9-13.

You, K., Flemings, P. B., Malinverno, A., Collett, T. S., & Darnell, K. (2019). Mechanisms of Methane Hydrate Formation in Geological Systems. *Reviews of Geophysics*, *57*(4). https://doi.org/10.1029/2018RG000638